
**A novel Quantum Gas Microscope for
Dysprosium Atoms:
Magnetic-Field Control and
Oven Characterization**

Paul Michael Uerlings

aus Stuttgart

Hauptberichter: Prof. Dr. Tilman PFAU

Mitberichter: Priv.-Doz. Dr. Eberhard GOERING

5. Physikalisches Institut

Universität Stuttgart

2021

Ehrenwörtliche Erklärung

Hiermit erkläre ich, dass ich diese Arbeit selbständig verfasst und keine anderen als die von mir angegebenen Quellen und Hilfsmittel verwendet habe.

Stuttgart, 29.10.2021

Paul Uerlings

Abstract

This thesis describes the design and characterization of several components of a novel quantum gas microscope for dysprosium atoms.

In the experimental apparatus, several magnetic-field coils are used in order to precisely control the magnetic field. Three large rectangular Helmholtz coil pairs are used to compensate external magnetic fields. A pair of circular Helmholtz coils designed is used to generate large homogeneous fields in the z -direction. A pair of circular coils in an anti-Helmholtz configuration is used in order to generate the quadrupole field needed for the operation of the magneto-optical trap. In this thesis, all of these coils are designed, wound and their magnetic fields are simulated.

A dual filament effusion cell consisting of an effusion cell (EC) and a hot lip (HL) is used to produce a hot atomic beam of dysprosium. The spatial profile of the atomic beam is measured using fluorescence imaging. The spatial profile is broader than expected, indicating that the atoms are emitted by the HL. The result is contrary to the assumed working principle of the effusion cell, where it is assumed that the atomic beam originates from the EC.

Contents

| | Page |
|---|-----------|
| Zusammenfassung | 1 |
| 1. Introduction | 5 |
| 2. Atom-Light Interaction | 7 |
| 2.1. Two-Level Atom | 7 |
| 2.1.1. Optical Bloch Equations | 10 |
| 2.1.2. Absorption in an Atomic Medium | 12 |
| 2.2. Broadening Mechanisms | 13 |
| 2.2.1. Homogeneous Broadening | 13 |
| 2.2.2. In-Homogeneous Broadening | 14 |
| 2.3. Spectroscopic Techniques | 18 |
| 2.3.1. Absorption Spectroscopy | 18 |
| 2.3.2. Fluorescence Spectroscopy | 19 |
| 2.4. Laser Cooling and Trapping | 20 |
| 2.4.1. Scattering Force | 20 |
| 2.4.2. Doppler Cooling | 21 |
| 2.4.3. Optical Molasses | 21 |
| 2.4.4. Magneto-Optical Trap | 22 |
| 3. Electromagnetism | 25 |
| 3.1. Biot-Savart Law | 26 |
| 3.2. Helmholtz Coil | 26 |
| 3.2.1. Anti-Helmholtz coil | 27 |
| 4. Interferometry | 31 |
| 4.1. Interference of two Plane Waves | 31 |
| 4.2. Michelson Interferometer | 32 |
| 5. Experimental Apparatus | 35 |
| 5.1. Magnetic Field Control | 37 |
| 5.1.1. Compensation Coils | 37 |
| 5.1.2. Gradient-/ and Feshbach Coils | 40 |

| | |
|--|-----------|
| 5.2. Manual Positioning Stage | 45 |
| 5.2.1. Characterization of the Z-Stage | 45 |
| 5.3. Transversal Cooling | 51 |
| 6. Atomic-Beam Spectroscopy | 53 |
| 6.1. Effusion Cell | 53 |
| 6.2. Atomic-Beam Characterization | 55 |
| 6.2.1. Transversal-Velocity Distribution | 57 |
| 6.2.2. Spatial Beam Profile | 57 |
| 6.2.3. Effusion-Cell Dynamics | 60 |
| 6.2.4. Summary | 66 |
| 7. Conclusion | 67 |
| Appendix | 69 |
| A. Winding the Magnetic-Field Coils | 69 |
| B. Magnetic-Field Simulation | 71 |
| Bibliography | 73 |
| Acknowledgments | 77 |

Zusammenfassung

Ausgelöst durch die ersten experimentellen Beobachtungen eines Bose-Einstein-Kondensats im Jahr 1995 [And+95][Dav+95] und eines entarteten Fermi-Gases im Jahr 1999 [DJ99], hat sich das Gebiet der ultrakalten Quantengase in den letzten zwei Jahrzehnten rasch weiterentwickelt. Das Abkühlen von Atomen auf ultrakalte Temperaturen und das Einfangen dieser in optischen Fallen ermöglicht eine außergewöhnliche Kontrolle der internen Freiheitsgrade des Systems. In Verbindung mit der Möglichkeit, die Wechselwirkung zwischen den Atomen mithilfe von Feshbach-Resonanzen zu modifizieren [Chi+10], bieten ultrakalte Quantengase eine leistungsstarke und vielseitige Plattform zur Untersuchung von Quanten-Vielteilchensystemen [And+97];[Mad+00];[Zwi+05]. Dipolare Quantengase sind von besonderem Interesse, da ihre Wechselwirkung über die Dipol-Dipol-Wechselwirkung zu völlig neuen Phänomenen wie selbstgebundenen Quantentröpfchen [Sch+16];[Kad+16] und suprafesten Arrays der Tröpfchen [Bö+19];[Guo+19];[Her+21] führt. In den letzten Jahren hat sich durch die Fortschritte bei der Erzeugung komplexer atomarer Vielteilchensysteme eine neue Art von Experimenten entwickelt, das sogenannte *Quantengasmikroskop*. In diesen Experimenten werden ultrakalte Atome in periodischen optischen Gitterpotentialen gefangen. Diese Systeme bieten eine ideale Plattform für die Untersuchung von Problemen aus der Festkörpertheorie, die vom Quantenmagnetismus bis zu Gitterspinmodellen und topologischer Materie reichen [Bak+09];[CI17]. Durch den Einsatz eines Quantengasmikroskops, das eine Einzelplatzauflösung ermöglicht, können mikroskopische Details wie Platz- und Spin-Korrelationen beobachtet werden. In dem hier vorgestellten Experiment werden Dysprosium-Atome in einem UV-optischen Gitter mit einem Gitterabstand von ca. 180 nm gefangen. In Verbindung mit der weitreichenden Dipol-Dipol-Wechselwirkung ($\propto 1/r^3$) erhöht der kleine Gitterabstand die Wechselwirkungsstärke zwischen den Atomen erheblich [Bai+16]. Dies ermöglicht es dem Experiment, in ein Regime stark wechselwirkender dipolarer Bose- und Fermi-Hubbard-Physik einzutreten, in dem sogar Wechselwirkungen zwischen den nächstgelegenen Nachbarn sichtbar werden könnten [Pik+10];[LKL15]. Das dipolare Fermi-Hubbard-Modell ist von besonderem Interesse, da man davon ausgeht, dass dieses Modell alle Eigenschaften eines Hoch-Temperatur-Supraleiters aufweist, wenn Dotierung und Temperatur variiert werden [Maz+17].

Diese Masterarbeit beschreibt den Aufbau und die Charakterisierung verschiedener Komponenten eines neuartigen Quantengasmikroskops für Dysprosiumatome.

In der Versuchsanordnung werden mehrere Magnetfeldspulen verwendet, um das Magnetfeld präzise zu steuern. Drei große rechteckige Helmholtz-Spulenpaare werden zur Kompensation externer Magnetfelder verwendet. Die Spulen sind so ausgelegt, dass sie jeweils ein

homogenes Magnetfeld in x-, y- und z-Richtung erzeugen. Das in der Mitte der Hauptkammer erzeugte Magnetfeld beträgt $B_{x/y/z} \approx 1 \text{ G/A}$. Die Kompensationsspulen können auch verwendet werden, um kleine Gradienten zu kompensieren. Ein Paar kreisförmiger Helmholtzspulen wird verwendet, um große homogene Magnetfelder in z-Richtung zu erzeugen. Sie werden auch als Feshbach-Spulen bezeichnet, da sie hauptsächlich zur Abstimmung von Atom-Atom-Wechselwirkungen über so genannte Feshbach-Resonanzen eingesetzt werden. Diese Spulen erzeugen ein Magnetfeld von $B_z \approx 1,5 \text{ G/A}$ und sind für den Betrieb bei Strömen $I > 50 \text{ A}$ ausgelegt. Ein Paar kreisförmiger Spulen in einer Anti-Helmholtz-Konfiguration wird verwendet, um das für den Betrieb der magneto-optischen Falle erforderliche Quadrupolfeld zu erzeugen. Der im Zentrum erzeugte Magnetfeldgradient beträgt $\nabla B_z \approx 1,5 \text{ (G/cm)/A}$ und $\nabla B_{x/y} \approx 0,7 \text{ (G/cm)/A}$. Im Rahmen dieser Arbeit wurden alle diese Spulen entworfen, gewickelt und ihre Magnetfelder simuliert.

In der Hauptkammer des Experiments ist ein hochauflösendes Abbildungssystem mit einer Auflösung von $r \approx 0,5 \mu\text{m}$ installiert. Das Objektiv wird mithilfe von mehreren Positioniertischen positioniert. Ein manueller Positioniertisch wird für die grobe Ausrichtung verwendet. In dieser Arbeit wurde dieser Positioniertisch mit interferometrischen Techniken charakterisiert. Der Positioniertisch hat einen Verfahrbereich von $d \pm 5 \text{ mm}$ und eine Auflösung von $r < 20 \mu\text{m}$. Die Stabilität der Kippwinkel während der Höhenverstellung beträgt $\Delta\alpha < 1,5 \text{ mrad}$ und die Langzeitstabilität des Tisches liegt bei $\Delta h < 500 \text{ nm}$ und damit in der Größenordnung der durch thermische Schwankungen verursachten Drifts.

Alle Experimente beginnen mit der Erzeugung eines heißen Atomstrahls aus Dysprosium. Dazu wird eine Doppelfilament-Effusionszelle verwendet, die aus einer Effusionszelle (EC), in der festes Dysprosium auf $T \approx 1100 \text{ °C}$ aufgeheizt wird, und einer heißen Apertur (HL) besteht, die wie eine beheizte Blende wirkt, um Verstopfungen der Zelle zu verhindern. In dieser Arbeit wurde das räumliche Profil des Atomstrahls mit spektroskopischen Techniken charakterisiert und der Einfluss verschiedener Temperaturen der EC und der HL bestimmt. Durch Absorptionsspektroskopie am 421 nm -Übergang von Dysprosium wurde die Transversalgeschwindigkeit des Atomstrahls auf $v_{\text{trans}} = 45(10) \text{ m/s}$ bestimmt. Mit Hilfe einer des Fluoreszenzbildgebung wurde das räumliche Strahlprofil des Atomstrahls gemessen. Die Messungen zeigen, dass die meisten Atome von der HL emittiert werden. Dies steht im Gegensatz zu dem angenommenen Funktionsprinzip der Effusionszelle, bei dem davon ausgegangen wird, dass der Atomstrahl aus der EC stammt. Infolgedessen ist der Atomstrahl viel breiter als erwartet und die transversalen Geschwindigkeiten sind größer.

Zum Zeitpunkt des Verfassens dieser Arbeit nähert sich das Experiment der Erzeugung

von ultrakalten Quantengasen in der Hauptkammer. Alle Spulen, die für die Magnetfeldkontrolle in der Hauptkammer benötigt werden, sind installiert. Mithilfe von spektroskopischen Messungen in der Hauptkammer wurden erste Anzeichen für eine transversale Abkühlung und eine longitudinale Verlangsamung des Atomstrahls beobachtet. Nachdem die Dysprosium-Atome erfolgreich in einer 5-Strahl-MOT eingefangen wurden, können die Positionierungstische für das hochauflösende Abbildungssystem installiert werden. In naher Zukunft wird die Glaszelle, die für das Quantengasmikroskop mit Einzelplatzauflösung benötigt wird, dem System hinzugefügt. Hier werden die Atome in einem optischen Gitter gefangen, um u.a. das dipolare Fermi-Hubbard-Modell zu untersuchen.

Chapter 1

Introduction

Sparked by the first experimental observation of a Bose-Einstein condensate in 1995 [And+95][Dav+95] and of a degenerate Fermi gas in 1999 [DJ99], the field of ultracold quantum gases has evolved rapidly in the past two decades. Cooling atoms to ultracold temperatures and trapping them in optical traps allows for extraordinary control of the systems' internal degrees of freedom. Combined with the ability to modify the interaction between the atoms using Feshbach resonances [Chi+10], ultracold quantum gases offer a powerful and versatile platform to study quantum many-body systems [And+97];[Mad+00];[Zwi+05]. Dipolar quantum gases are of particular interest because the interaction via the dipole-dipole interaction has led to totally new phenomena like self-bound quantum droplets [Sch+16];[Kad+16] and supersolid arrays of droplets [Bö+19];[Guo+19];[Her+21]. In the recent years, fuelled by the progress in the creation of complex atomic many-body systems, a new type of technique, called *quantum gas microscopy* emerged. In these experiments, ultracold atoms are trapped in periodic optical lattice potentials. These systems offer an ideal platform to study problems from solid-state theory ranging from quantum magnetism to lattice spin models and topological matter [Bak+09];[CI17]. By implementing a quantum gas microscope which will enable single-site resolution, microscopic details such as site and spin correlations can be observed. In the experiment presented in this thesis dysprosium atoms will be trapped in an UV optical lattice with a lattice spacing of $a \approx 180$ nm. Combined with the long-range dipole-dipole interaction ($\propto 1/r^3$), the small lattice spacing significantly increases the interaction strength between atoms [Bai+16]. This allows the experiment to enter a regime of strongly interacting dipolar Bose- and Fermi-Hubbard physics where even next-nearest neighbour interactions could become visible [Pik+10];[LKL15]. The dipolar Fermi-Hubbard model is of particular interest as this model is thought to have all the same as a high- T_c superconductor when the doping and temperature are varied [Maz+17].

Outline of this thesis

In this thesis, some of the components that are used in the quantum gas microscope are set up and characterized. Additionally the spatial profile of the atomic beam is measured. In **Chapter 2** the theoretical aspects of the interaction between atoms and light is discussed. In a next step, spectroscopic techniques and broadening mechanisms are introduced. These techniques will be used later in order to characterize the atomic beam. In **Chapter 3** is derived how classical electromagnetism can be used in order to calculate the magnetic field generated by a coil. These principles are used to simulate the field generated by various coils used in the experimental apparatus.

Chapter 4 gives a brief introduction into interferometry and how a Michelson interferometer can be used in order to extract information of an underlying system.

In **Chapter 5** the experimental apparatus is described. In the scope of this thesis several components are designed and set up. These components are characterized and discussed in more detail. First, the different coils that are used for the magnetic-field control of the experiment are introduced. The magnetic field generated by the individual coils is simulated before winding them. Second, the mechanical properties of a manual positioning stage are measured using a Michelson interferometer. The short- and long-term stability is measured.

Chapter 6 describes the characterization of the atomic beam. The spatial profile of the atomic beam is measured using fluorescence spectroscopy. The influence of different temperatures of the dual filament effusion cell on the spatial profile of the beam is determined.

Atom-Light Interaction

To understand some of the fundamentals of atom-light interactions in this chapter, the atom is treated using quantum mechanically while the description of the electric field is kept classical. In order to simplify this introduction into atom-light interactions, an atom with only two discrete levels is used¹. First, the interaction of light with a single atom is discussed in the context of the optical Bloch equations. In a next step, the absorption of an atomic medium and line-broadening mechanisms are derived. The two different spectroscopic techniques that are used in order to characterize the atomic beam are introduced. To conclude, optical cooling and trapping techniques such as Zeeman-slowing and magneto-optical trapping are described.

2.1. Two-Level Atom

The two-level atom is an idealized description of an atom. The level structure of real atoms is much more complicated. However, because of selection rules that only allow certain transitions this multitude of states can effectively be reduced to a two-level system. The Hamiltonian H_A of such a two-level atom is given by

$$H_A = E_g |g\rangle \langle g| + E_e |e\rangle \langle e| , \quad (2.1)$$

where $|g\rangle$ is the ground state, $|e\rangle$ is the excited state and $E_n = \hbar\omega_n$ are the corresponding eigenenergies. The level structure of such a two-level atom is depicted in Figure 2.1. The energy difference between the excited state and the ground state is given by $\Delta E = \hbar\omega_0$. A light field with the energy $E = \hbar\omega$ drives transitions between the ground and excited state. The excited state can decay by spontaneous emission at a decay rate denoted by Γ . An electric field oscillating at a frequency $\omega = 2\pi f$ and described by

$$\mathbf{E} = \mathbf{E}_0 \cos(\omega t) , \quad (2.2)$$

¹ The derivation follows the ones done in [Foo05], [Dem13].

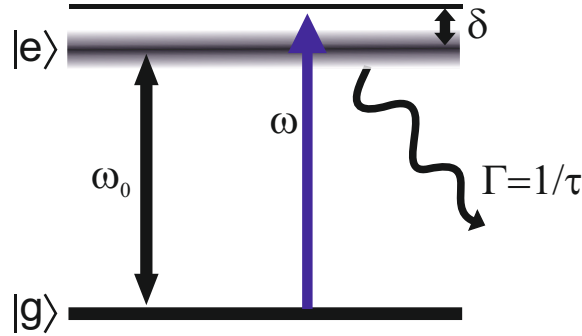


Figure 2.1.: Level structure of a two-level atom. The atom has an energetic groundstate denoted by $|g\rangle$ and an excited state denoted by $|e\rangle$. The energy difference between the two states is given by $\Delta E = \hbar\omega_0$. A light field oscillating at a frequency ω that is detuned from the atomic resonance by δ drives transitions between the ground and excited state. The excited state has a lifetime τ and decays back to the ground state by spontaneous emission at a decay rate denoted by $\Gamma = 1/\tau$.

describes the light field. The interaction between the atom and the light field is treated using time-dependent perturbation theory. The perturbation caused by the oscillating electric field is described by the interaction Hamiltonian H_I

$$H_I(t) = e\mathbf{r} \cdot \mathbf{E}_0 \cos(\omega t). \quad (2.3)$$

This Hamiltonian corresponds to the energy of an electric dipole with dipole moment $\mathbf{d} = -e\mathbf{r}$ in an oscillating electric field. The electric dipole moment arises from a single electron at a position \mathbf{r} with respect to the atomic nucleus. For the unperturbed atom, the wavefunction for the level n with energy E_n can be written as

$$\Psi_n(\mathbf{r}, t) = \psi_n(\mathbf{r}) \exp\left(\frac{-iE_n t}{\hbar}\right), \quad (2.4)$$

were the spatial wavefunctions satisfy $H_0\psi_n = E_n\psi_n$. These wavefunctions are not stationary solutions of the full Hamiltonian described by

$$H = H_A + H_I(t). \quad (2.5)$$

In order to describe the full system, a time-dependent constant $c_n(t)$ is included in Eq. (2.4),

$$\Psi(\mathbf{r}, t) = c_g(t) |g\rangle \exp\left(\frac{-iE_g t}{\hbar}\right) + c_e(t) |e\rangle \exp\left(\frac{-iE_e t}{\hbar}\right). \quad (2.6)$$

Normalization of this wavefunction requires that the two time-dependent coefficients satisfy

$$|c_g|^2 + |c_e|^2 = 1, \quad (2.7)$$

where $|c_g|^2$ and $|c_e|^2$ are the diagonal elements of the *density matrix*

$$|\Psi\rangle\langle\Psi| = \begin{pmatrix} |c_g|^2 & c_g c_e^* \\ c_e c_g^* & |c_e|^2 \end{pmatrix} = \begin{pmatrix} \rho_{gg} & \rho_{ge} \\ \rho_{eg} & \rho_{ee} \end{pmatrix}. \quad (2.8)$$

The diagonal elements ρ_{gg} and ρ_{ee} are the populations of the respective states. The off-diagonal elements ρ_{eg} and ρ_{ge} are called coherences.

In order to describe the system as a function of time, the time-dependent *Schrödinger equation* is used

$$i\hbar \frac{\partial\Psi}{\partial t} = H\Psi, \quad (2.9)$$

with the reduced Planck's constant \hbar . Substituting Eq. (2.6) into the Schrödinger equation leads to a set of coupled differential equations

$$\begin{aligned} i\dot{c}_g &= \Omega \cos(\omega t) \exp(-i\omega_0 t) c_e, \\ i\dot{c}_e &= \Omega^* \cos(\omega t) \exp(i\omega_0 t) c_g, \end{aligned} \quad (2.10)$$

where $\omega_0 = (E_e - E_g) / \hbar$ and Ω is the Rabi frequency. Without loss of generality, the light is assumed to be linearly polarized along the x-axis. The Rabi frequency is then given by

$$\Omega = \frac{e \langle g | x | e \rangle |\mathbf{E}_0|}{\hbar}. \quad (2.11)$$

The Rabi frequency is a measure of the coupling strength between the light and the atomic transition. It is proportional to the amplitude of the light field. In order to obtain this result the *dipole* approximation is used. The electric field is assumed to be uniform over the atomic wavefunction, simplifying the calculations. The dipole approximation is justified if the radiation has a wavelength much larger than the size of the atom ($\lambda \gg a_0$).

2.1.1. Optical Bloch Equations

The dipole moment induced on the atom by this light field is given by the expectation value

$$-eD_x(t) = - \int d^3\mathbf{r} \Psi^\dagger(t) ex \Psi(t). \quad (2.12)$$

Here, the electric field is again assumed to be linearly polarized along the x-axis. Substituting the wavefunction of the two-level atom derived previously in Eq. (2.6) gives the dipole moment of the atom as

$$D_x(t) = c_e^* c_g X_{eg} \exp(i\omega_0 t) + c_g^* c_e X_{ge} \exp(-i\omega_0 t) \quad (2.13)$$

where

$$X_{ge} = \langle g | x | e \rangle, \quad (2.14)$$

and $c_e^* c_g = \rho_{eg}^*$ and $c_g^* c_e = \rho_{ge}^*$ are the coherences described by the density matrix in Eq. (2.8). In order to describe the time evolution in the case of an atom interacting with a light field, new variables are introduced using [Foo05]

$$\begin{aligned} \tilde{c}_g &= c_g \exp(-i\delta t/2), \\ \tilde{c}_e &= c_e \exp(i\delta t/2), \end{aligned} \quad (2.15)$$

with the detuning $\delta = \omega - \omega_0$ between the driving light field and the atomic resonance. This transformation is justified as it does not affect the populations ($\tilde{\rho}_{ee} = \rho_{ee}$). However the coherences become $\tilde{\rho}_{eg} = \rho_{eg} \exp(-\delta t)$ and $\tilde{\rho}_{ge} = \rho_{ge} \exp(\delta t)$ [Foo05]. In terms of these new variables the dipole moment is

$$D_x(t) = X_{ge} (u \cos(\omega t) - v \sin(\omega t)), \quad (2.16)$$

with

$$\begin{aligned} u &= \tilde{\rho}_{ge} + \tilde{\rho}_{eg}, \\ v &= -i(\tilde{\rho}_{ge} - \tilde{\rho}_{eg}). \end{aligned} \quad (2.17)$$

In order to find expressions for $\tilde{\rho}_{ge}$ and $\tilde{\rho}_{eg}$, Eq. (2.10) has to be solved. The result is a compact set of equations [Foo05]:

$$\begin{aligned}\dot{u} &= \delta v, \\ \dot{v} &= -\delta u + \Omega w, \\ \dot{w} &= -\Omega v,\end{aligned}\tag{2.18}$$

with the population difference between the ground state and the excited state $w = \rho_{ee} - \rho_{gg}$. These equations describe the coherent evolution of the two states and thus spontaneous decay is ignored. In general this treatment is not justified as spontaneous decay of the excited state occurs on a much faster timescale than any coherent process and therefore washes out the coherent evolution of the states [Foo05]. In analogy to a classical oscillator this decay can be introduced by a damping term

$$\dot{\rho}_{ee} = -\Gamma\rho_{ee} + \frac{\Omega}{2}v,\tag{2.19}$$

where the excited state decays by spontaneous emission with a lifetime of $\tau = 1/\Gamma$. As a direct result of this damping term the excited state will decay back to the ground state in the absence of a driving light field ($\Omega = 0$). Substituting the damping given in Eq. (2.19) into Eq. (2.18) results in a new set of equations also known as the *optical Bloch equations*

$$\begin{aligned}\dot{u} &= \delta v - \frac{\Gamma}{2}u, \\ \dot{v} &= -\delta u + \Omega w - \frac{\Gamma}{2}v, \\ \dot{w} &= -\Omega v - \Gamma(w - 1).\end{aligned}\tag{2.20}$$

These equations describe the of light with the two-level atom close to resonance. The detuning δ and Rabi frequency Ω fully describe the driving light field. The excited state has a lifetime of $\tau = 1/\Gamma$ and decays by spontaneous emission. The optical Bloch equations describe the full dynamics of a two-level atom interacting with a driving light field.

Steady-state solution of the optical Bloch equations

In the case where times are long compared to the lifetime of the excited state ($t \gg \Gamma^{-1}$) the steady-state solution, where $\dot{u} = \dot{v} = \dot{w} = 0$, is given by [Foo05]

$$\begin{aligned} u &= \frac{\Omega\delta}{\delta^2 + \Omega^2/2 + \Gamma^2/4}, \\ v &= \frac{\Omega\Gamma/2}{\delta^2 + \Omega^2/2 + \Gamma^2/4}, \\ w &= \frac{\delta^2 + \Gamma^2/4}{\delta^2 + \Omega^2/2 + \Gamma^2/4}. \end{aligned} \tag{2.21}$$

The excited-state population is given by

$$\rho_{ee} = \frac{1 - w}{2} = \frac{\Omega^2/4}{\delta^2 + \Omega^2/2 + \Gamma^2/4}. \tag{2.22}$$

For a strong driving field ($\Omega \rightarrow \infty$), the populations in the two states equalize and $\rho_{ee} \rightarrow 1/2$. The saturation intensity I_{sat} is defined as the minimum intensity that tends to equalize the populations [Foo05]. It is given by

$$\frac{I}{I_{\text{sat}}(\omega)} = \frac{2\Omega^2}{\Gamma^2}. \tag{2.23}$$

At resonance ($\delta = 0$) the saturation intensity is given by

$$I_{\text{sat}} = \frac{\pi}{3} \frac{hc}{\lambda^3 \tau}, \tag{2.24}$$

with the speed of light c , the wavelength at resonance λ .

2.1.2. Absorption in an Atomic Medium

The derivation described above was done for a single atom interacting with a light field. In an atomic beam, the collective response of the atomic medium has to be considered. As the light passes through the medium of thickness z it gets absorbed. The intensity of the light

$$I(\omega, z) = I(\omega, z = 0) \exp(-\kappa(\omega)z), \tag{2.25}$$

is therefore attenuated. The absorption coefficient $\kappa(\omega)$ is given by

$$\kappa(\omega) = (N_g - N_e)\sigma(\omega), \quad (2.26)$$

where N_g and N_e are the populations in the ground state and excited state, respectively. They are related to the density matrix described in Eq. (2.8) by $\rho_{ee} = N_e/N$, where $N = N_e + N_g$ is the number of atoms per unit volume in the atomic medium. The absorption cross-section $\sigma(\omega)$ is given by [Foo05]

$$\sigma(\omega) \propto \frac{1}{2\pi} \frac{\Gamma}{\delta^2 + \Gamma^2/4}. \quad (2.27)$$

The resulting absorption profile can therefore be described by a Lorentzian line-shape function. The full width at half maximum (FWHM) of the Lorentzian depends on the decay rate Γ of the atomic transition. When dealing with absorption profiles of atomic transitions the FWHM is often referred to as the linewidth of a transition. The broadening that is caused by the spontaneous emission of the excited state is called *radiative broadening*.

2.2. Broadening Mechanisms

There are several mechanisms that lead to a broadening of the atomic transition lines when performing spectroscopy. They can be grouped into homogeneous and inhomogeneous broadening mechanisms. Homogeneous effects affect all atoms the same leading to a line shape that can be described by a Lorentzian. In-homogeneous effects affect different classes of atoms by different amounts. In-homogeneous effect lead to a Gaussian line shape. In the following sections only the broadening mechanisms that are important for atomic beam spectroscopy are introduced and discussed.

2.2.1. Homogeneous Broadening

One example for homogeneous broadening is the *radiative broadening* introduced in Chapter 2.1.2. Radiative broadening solely depends on the decay rate of the excited state Γ . As the decay rate is inversely proportional to the lifetime τ ($\tau = \Gamma^{-1}$), the longer the lifetime of the excited state, the more narrow the transition becomes.

The absorption coefficient κ introduced in Chapter 2.1.2 also has a dependency on the

intensity of the light field given by [Foo05]

$$\kappa(\omega, I) = N\sigma_0 \frac{\frac{\Gamma^2}{4}}{\delta^2 + \frac{\Gamma^2}{4}(1 + I/I_{\text{sat}})}. \quad (2.28)$$

This expression for the absorption coefficient again has a Lorentzian line shape. The linewidth (FWHM) of the Lorentzian is given by

$$\Delta\omega_{\text{FWHM}} = \Gamma \left(1 + \frac{2\Omega^2}{\Gamma^2}\right)^{1/2} = \Gamma \left(1 + \frac{I}{I_{\text{sat}}}\right)^{1/2}. \quad (2.29)$$

For a weak light field ($I < I_{\text{sat}}$) the linewidth is dominated by radiative broadening and depends only on Γ . For a strong light field ($I \gg I_{\text{sat}}$) this is no longer the case. By increasing the intensity of the light field the transitions broadens. This effect is known as *power broadening*. The absorption coefficient $\kappa(\omega, I)$ as a function of the frequency of the light field ω is depicted in Figure 2.2. The figure shows $\kappa(\omega, I)$ for different values of the decay rate Γ and intensity of the light field I . In Figure 2.2 a), the decay rate Γ is varied while the intensity is kept constant. For larger Γ (and thus shorter lifetimes) the absorption profile broadens. In Figure 2.2 b) and c), the intensity I is varied and the decay rate is kept constant. For increasing intensity ($I \gg I_{\text{sat}}$) the linewidth of the absorption profile increases according to Eq. (2.29).

2.2.2. In-Homogeneous Broadening

The most important in-homogeneous broadening mechanism when dealing with atomic beam spectroscopy is *doppler broadening*. In the reference frame of an atom moving with a velocity \mathbf{v} the frequency of the light appears shifted. This shifted frequency ω' is given by

$$\omega' = \omega - \mathbf{k} \cdot \mathbf{v}, \quad (2.30)$$

where ω is the frequency of the light in the rest frame and \mathbf{k} is the wave vector of the incident light. For a stationary atom the resonance frequency is given by ω_0 . As a result of the Doppler shift, ω_0 appears to shift towards higher or lower frequencies depending if the atom is moving towards or away from the light respectively. This phenomenon is known as the *Doppler shift*.

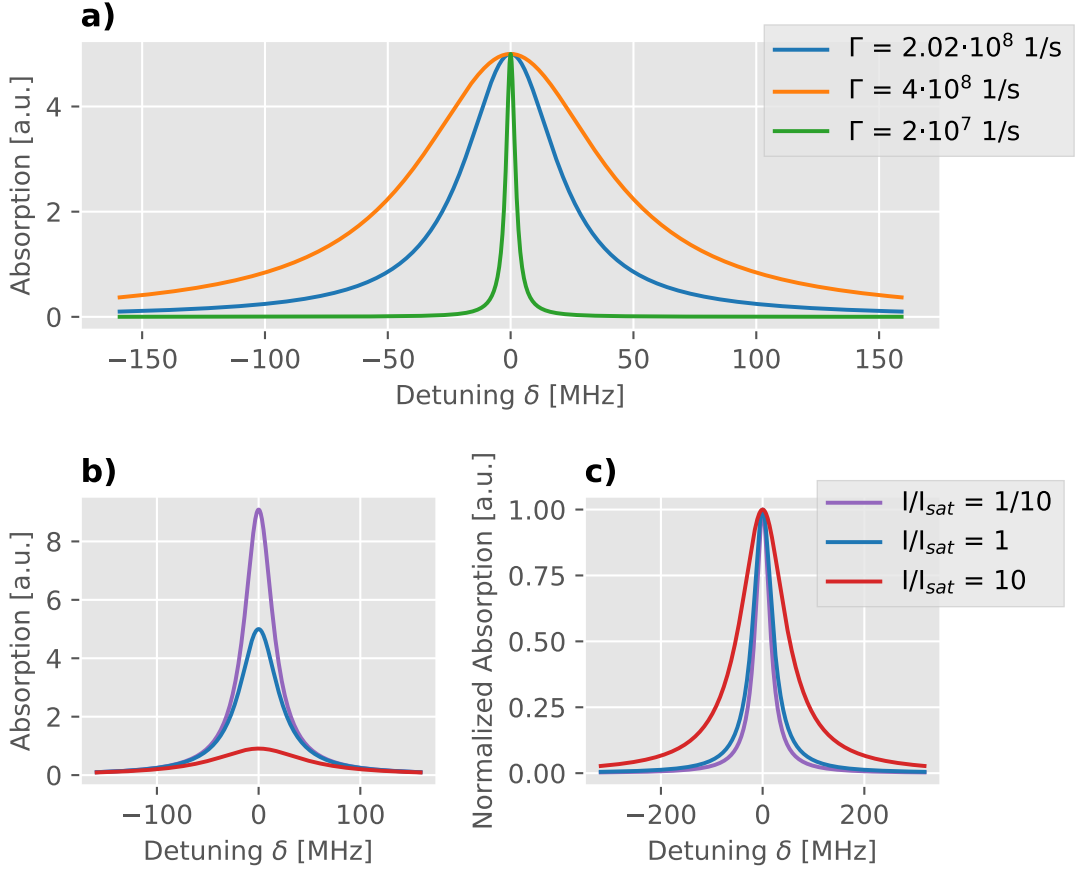


Figure 2.2.: The absorption coefficient as a function of the detuning from resonance for different parameters Γ and I . The absorption profiles are calculated using Eq. (2.28). In a) the intensity is set to $I/I_{\text{sat}} = 1$ and the decay rate Γ is varied. For smaller Γ (longer lifetime of the excited state) the linewidth is significantly reduced. This effect is known as radiative broadening. In b) and c) the decay rate is set to $\Gamma = 2.02 \cdot 10^8$ 1/s and the intensity is varied. The profile c) are normalized in order to make the change in linewidth more visible. With increasing power ($I \gg I_{\text{sat}}$) the transition broadens. This effect is known as power broadening. Note that the blue profile is always calculated using the same parameters and serves as a reference.

In equilibrium, thermal atoms have a velocity distribution described by the Maxwell-Boltzmann distribution

$$p(v_i, T) = \sqrt{\frac{m}{2\pi k_B T}} \exp\left(-\frac{mv_i^2}{2k_B T}\right), \quad v_i \in [v_x, v_y, v_z] \quad (2.31)$$

where $p(v_i, T)$ is the probability to find an atom with velocity v_i for a given temperature T , m is the mass of the atom and k_B is the Boltzmann constant. It is often also interesting

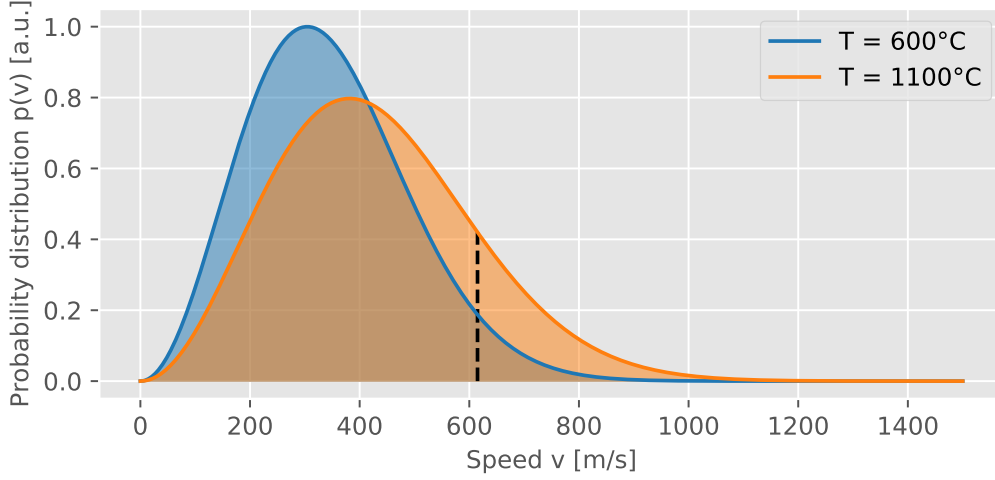


Figure 2.3.: Speed distribution of dysprosium atoms given by the Maxwell-Boltzmann distribution (Eq. (2.32)). In the case of 162-dysprosium the mass is set to $m = 162 \cdot 1.6 \cdot 10^{27}$ kg. In the experiment the effusion cell is typically set to $T = 1100^\circ\text{C}$. In the case of an atomic beam emerging from an effusion cell this speed can be used in order to approximate the longitudinal velocity of the atoms leaving the oven. For a reference, the capture velocity of the Zeeman-slower used in the experiment is indicated by a dashed line.

to look at the probability to find an atom with the speed $v = \sqrt{v_x^2 + v_y^2 + v_z^2}$

$$p(v, T) = 4\pi \left(\frac{m}{2\pi k_B T} \right)^{3/2} v^2 \exp\left(-\frac{mv^2}{2k_B T}\right). \quad (2.32)$$

For 162-dysprosium the mass is $m = 162 \cdot 1.6 \cdot 10^{27}$ kg and the corresponding distribution is depicted in Figure 2.3. For increasing temperatures the maximum of the probability distribution shift towards higher velocities. The most probable speed for any given temperature can be calculated using [Dem07]

$$v_{\text{mp}}(T) = \sqrt{\frac{2k_B T}{m}}. \quad (2.33)$$

The mean velocity is given by [Dem18]

$$v_{\text{mean}} = \frac{2v_{\text{mp}}}{\sqrt{\pi}}. \quad (2.34)$$

For the typical operating temperature of the effusion cell used in the experiment ($T = 1100^\circ\text{C}$) the most probable speed is $v_{\text{mp}(T=1373\text{K})} \approx 380$ m/s, and the mean velocity is $v_{\text{mean}} \approx 430$ m/s.

As thermal atoms are moving with a velocity described by the Maxwell-Boltzmann distribution. The atoms experience a frequency shift that depends on their individual velocity and can be calculated using Eq. (2.30). By including this velocity dependent shift into Eq. (2.28) and by integrating over all velocity classes and weighting them according to Maxwell-Boltzmann distribution (Eq. (2.31)) the Doppler broadened profile can be obtained. Such a profile is shown in Figure 2.4. Compared to the profile that is dominated by radiative broadening (orange profile), the Doppler broadened profile (blue profile) has a linewidth that is approximately two orders of magnitude larger. The regime where the Doppler broadening dominates the profile is referred to as *Doppler limited*. In a regime where the Doppler broadening dominates the line shape is given by [Dem07]

$$I(\omega) = I(\omega_0) \exp \left[- \left(\frac{\omega - \omega_0}{\omega_0 v_{\text{mp}}(T)/c} \right)^2 \right]. \quad (2.35)$$

Since the Gaussian profile approaches zero faster than the Lorentzian profile, for a large detuning δ the pure Doppler profile (black dashed line in Figure 2.4) differs from the one calculated using Eq. (2.28) [Dem07].

For the fast atoms in a hot atomic beam the transit time t of the atoms moving through the light can be calculated using $t = d/v$, where d is the diameter of the light beam and v is the velocity of the atom perpendicular to the light. In the case where $t \gg \Gamma^{-1}$ the linewidth is dominated by the radiative broadening. However, for $t \sim \Gamma^{-1}$, the transit time t limits the linewidth. The resulting Gaussian line profile is given by [Dem07]

$$I(\omega) = I_0 \exp \left(-\delta^2 \frac{w^2}{2v^2} \right), \quad (2.36)$$

where w is the waist of the light beam and v is the velocity of the atoms perpendicular to the light. This effect is known as *transit-time broadening*.

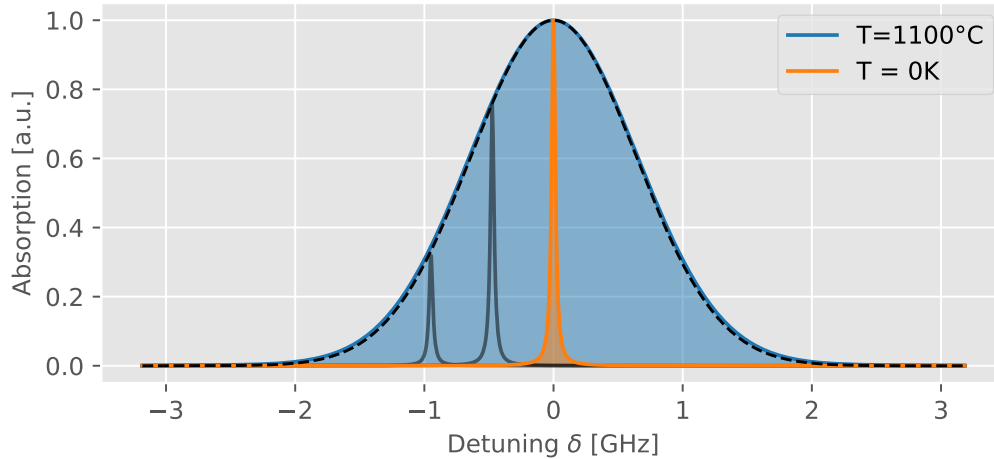


Figure 2.4.: Normalized Doppler profile for the 421 nm transition in dysprosium calculated by a weighted sum over all velocities according to Eq. (2.31). The individual profiles are obtained using Eq. (2.28) and setting $I = I_{\text{sat}}/10$ in order to let power broadening play a negligible role. The blue profile is calculated for a temperature of $T = 1100^\circ\text{C}$. The grey lines indicate the profiles for the individual velocities which are summed up in order to obtain the full Doppler profile. Each individual profile is radiation broadened with a FWHM given by Eq. (2.29). The orange profile is calculated for $T = 0\text{K}$ and is thus no Doppler broadening occurs. The profile is comparable to the ones shown in Figure 2.2. Compared to the Doppler broadened profile the FWHM is reduced by a factor of ~ 10 . The black dashed line shows a Gaussian Doppler profile which is calculated using Eq. (2.35).

2.3. Spectroscopic Techniques

In order to detect the absorption profiles discussed in the previous chapter, various experimental techniques can be used. These spectroscopic techniques allow for the detection of atomic transitions and are used to obtain the spectral information. In order to do so, either the frequency of the light has to be tunable² or an optical spectrometer has to be used. In the following, two techniques namely, absorption spectroscopy and fluorescence spectroscopy are introduced and discussed.

2.3.1. Absorption Spectroscopy

One of the simplest methods to measure the absorption profiles discussed in Chapter 2.2 is to use a single light beam incident with the atoms and detecting the transmitted light. This technique is known as *absorption spectroscopy* and a schematic of the setup is shown in Figure 2.5. As the laser frequency is tuned closer to resonance, more light is absorbed

² Also, the linewidth of the laser has to be narrow compared to the atomic transition.

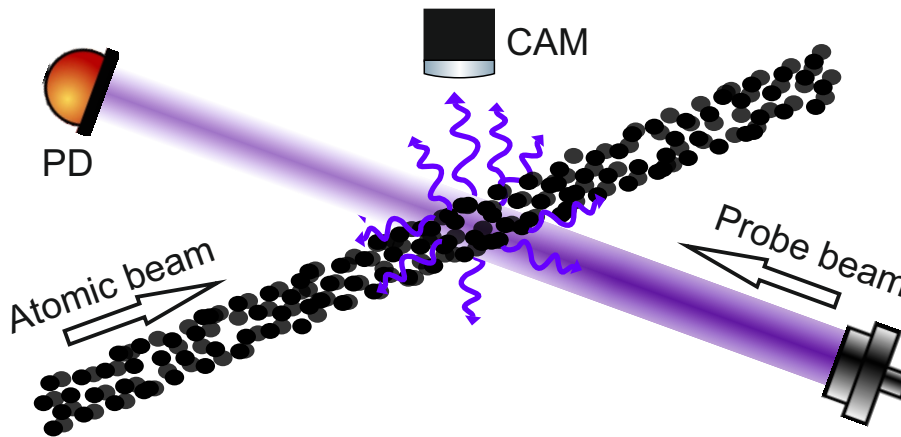


Figure 2.5.: Schematic of a setup that is used for spectroscopic measurements. A probe beam is incident with the atomic beam. If the light is close to the atomic resonance the atoms absorb parts of the light. A photodiode (PD) can be used to detect the probe beam after it has passed through the atomic beam. If the frequency of the probe beam is tuned closer to the atomic resonance, more light is absorbed by the atoms and the intensity of the detected light decreases. After the atoms absorb the probe light they decay back to their ground state by spontaneous emission, emitting light in all directions. A camera (CAM) can be used to detect this fluorescence. On resonance, a maximum in the fluorescence signal is measured.

by the atoms. Thus, on resonance a minimum in the transmitted signal can be observed. For a weak probe power ($I \leq I_{\text{sat}}$) the profile obtained by absorption spectroscopy is Doppler limited. A typical Doppler broadened absorption profile is shown in Figure 2.4. As it requires only a limited number of parts, absorption spectroscopy is ideal in order to perform fast checks on a system or when working with limited available optical access. However, as absorption spectroscopy is Doppler limited, it cannot be used in order to gain insights on the fine details of atomic transitions such like the fine or hyperfine structure of an atomic transition. Because the linewidth is limited by the Doppler broadening, which depends on the temperature of the atoms, absorption spectroscopy can be used in order to determine the velocity distribution.

2.3.2. Fluorescence Spectroscopy

When excited atoms decay back to lower energy states, they emit light in all directions. This fluorescence can be measured and results in a profile equivalent to that of the absorption spectroscopy described above. A schematic of the setup used for fluorescence spectroscopy is depicted in Figure 2.5. As the laser is tuned to the atomic resonance more atoms get excited to the excited state and more light is emitted when they decay

back to the ground state. Therefore, on resonance a maximum in the fluorescence signal is detected. Like absorption spectroscopy, fluorescence spectroscopy is Doppler limited. By detecting the fluorescence with a camera, the spatial profile of for example an atomic beam can be measured.

2.4. Laser Cooling and Trapping

In the previous chapter it was discussed how atoms interact with light and how the absorption spectrum in an hot atomic medium is limited by the Doppler broadening. Even at room temperature the atoms in an atomic beam or vapor have speeds in the hundreds of meters per second³. As a result, the Doppler broadening dominates over other broadening mechanisms. For many experiments it is therefore desirable to slow down the atomic beam, i.e. cooling the atoms. There are several mechanisms that can be used in order to slow down atoms, one of which is the *scattering force*. In the following sections the scattering force is introduced and its applications will be discussed.

2.4.1. Scattering Force

The scattering force is the result of the absorption and subsequent emission of photons by a single atom. Each photon carries a momentum $p = \hbar k = h/\lambda$. As the momentum is always conserved, if an atom absorbs a photon, the photon transfers its momentum to the atom. The opposite is true if an excited atom emits a photon as a result of decaying back to the ground state. The force exerted on the atom is given by [Foo05]

$$\mathbf{F}_{\text{scatt}} = \hbar \mathbf{k} \cdot R_{\text{scatt}}, \quad (2.37)$$

with the wave vector \mathbf{k} and the scattering rate $R_{\text{scatt}} = \Gamma \rho_{ee}$. ρ_{ee} is the excited state population which was already introduced in Chapter 2.1.1. Substitution of Eq. (2.22) into Eq. (2.37) gives

$$\mathbf{F}_{\text{scatt}} = \hbar \mathbf{k} \cdot \Gamma \frac{\Omega^2/4}{\delta^2 + \Omega^2/2 + \Gamma^2/4}, \quad (2.38)$$

where the detuning includes the Doppler shift and is given by $\delta = \omega - \omega_0 + kv$. For strong laser intensities (i.e. $\Omega \rightarrow \infty$) the scattering force approaches $F_{\text{max}} = \hbar k \Gamma / 2$. The resulting

³ For Dy-Atoms and using Eq. (2.33), the most probable speed for a temperature of $T = 20^\circ\text{C}$ is $v_{\text{mp}(T)} \approx 170 \text{ m/s}$.

acceleration is $a_{\max} = F_{\max}/m$, with the mass of the atom m ⁴. The scattering force can be used in order to slow down atoms. In the case of one laser beam counter propagating to an atomic beam, the atoms absorb photons from one direction only. However, if the excited atoms decay back to their ground state they can emit the photon in all directions. As a result of this, a net force is exerted on the atom, slowing it down.

2.4.2. Doppler Cooling

The scattering force is dependent on the detuning δ , the force applied to the atoms strongly depends in their velocity (see Eq. (2.38)). Figure 2.6 shows the scattering force as a function of velocity for a red-detuned laser. At the velocities where the detuning of the of the laser cancels out the detuning caused by the Doppler shift the force has its maximum. As the atoms get decelerated by the scattering force, the Doppler shift decreases. As a result, the atoms are slowed down until the Doppler shift takes them so far out of resonance that the scattering rate is not sufficient for slowing them down further. One way to overcome this limitation is by continuously tuning the laser frequency such that it stays resonant while the atoms are slowed down. Alternatively, the atomic transition can be shifted using the Zeeman-shift. Here, the atomic transition is shifted by a magnetic field⁵. If the magnetic field strength is varied according to the deceleration of the atoms, the laser can be kept on resonance until the atoms come to a stop.

2.4.3. Optical Molasses

In the previous section, the scattering force as a result of one laser beam incident with the atoms was discussed. By using two opposing, red-detuned laser beams incident with the atoms the scattering force can be tuned to be proportional to the velocity resulting in viscous damping of the atoms. This is know as an *optical molasses* (OM) [MS99]. As the atoms move in one direction, in the rest frame of the atom, one of the laser beams will be slightly red shifted while the other laser will be shifted towards the blue. If the laser is red-detuned, atoms will interact more strongly with the laser beam that opposes their velocity. As a result the atoms are slowed down. This is depicted in Figure 2.7. The same phenomenon can also be achieved in three dimensions. In this case the motion in all directions is slowed down and collecting the atoms in a small region. The scattering force does not depend on the position of the atoms. Due to the lack of spatial confinement,

⁴ For dysprosium atoms and using the 421 nm transition $a_{\max} \approx 6 \cdot 10^5$ m/s.

⁵ This is known as a Zeeman-Slower. Alternatively the Stark-effect can be used in order to shift the atomic transition. Here the electric field is altered.

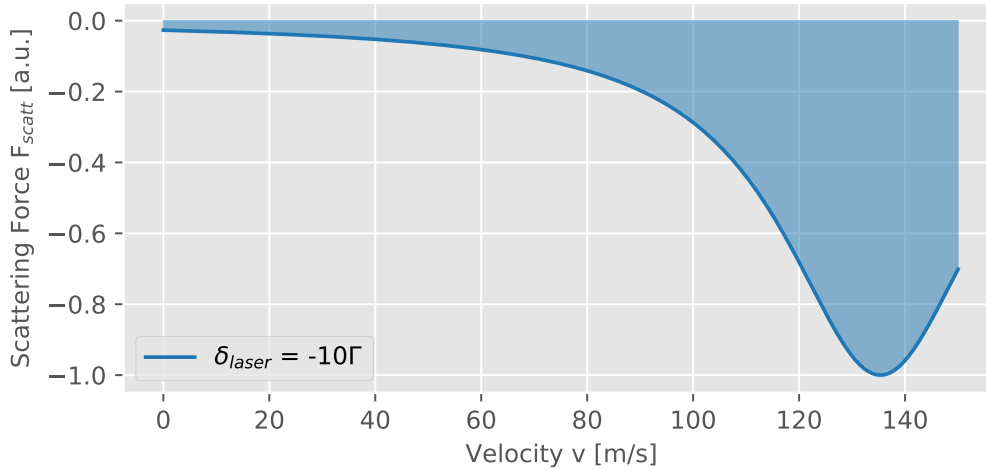


Figure 2.6.: The scattering force as a function of velocity of the atom for one laser beam incident with the atoms. The force is calculated for dysprosium atoms and a laser tuned close to the blue 421 nm transition. The laser is red-detuned from the atomic transition by $\delta_{laser} = -10\Gamma$. Atoms that are counter-propagating with respect to the wave vector \mathbf{k} of the laser (positive velocities) experience a Doppler shift that shifts the laser in the blue (i.e. closer so resonance). The atoms experience a decelerating force that depends on their velocity. By tuning the laser frequency the maximum of the scattering force can be shifted to different velocities.

atoms can still slowly drift away. Such a system is therefore not a optical trap for atoms. Still, the detainment time of atoms inside an optical molasses can be remarkably long [MS99].

2.4.4. Magneto-Optical Trap

In order to trap atoms, there has to be a force applied to the atoms has to depend on their position. One way to apply such a force is by using a *magneto-optical trap* (MOT). The operation of a MOT relies on the Zeeman-shift described earlier. An inhomogeneous magnetic field shifts the atomic transition depending on the position. The force applied points towards the trap center. As is the case with the optical molasses, counter-propagating laser beams provide a scattering force. The force applied is analogous to the velocity damping in the case of an optical molasses. The difference being, that in the former the Doppler effect changes the force where in the case of the MOT the change is due to the Zeeman-shift. By making use of three counter-propagating laser beams and by applying a magnetic field gradient in all three directions, a MOT can trap atoms in all three dimensions. In the case of a MOT operating on the 626 nm transition in dysprosium, $N > 10^8$ atoms can be trapped at temperatures $T < 500 \mu\text{K}$ [Mai15].

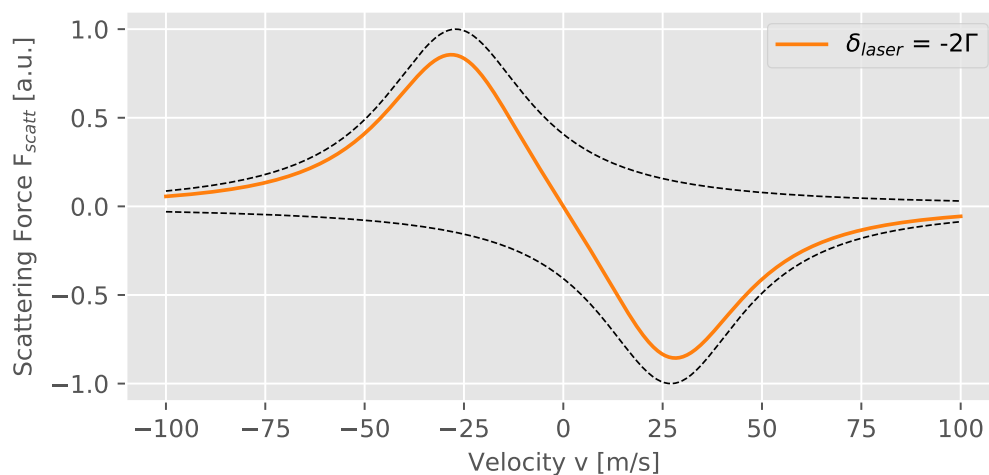


Figure 2.7.: Scattering force as a function of velocity of the atom for a 1-dimensional optical molasses. The scattering force is calculated in the case of dysprosium atoms using the blue 421 nm transition. The two laser beams are red-detuned from the atomic transition by $\delta_{\text{laser}} = -2\Gamma$. The two dotted lines show the scattering force from the two individual laser beams. The orange line shows the total force. Atoms traveling at velocities $v > 0$ experience a decelerating force. The opposite is true for atoms moving with velocities $v < 0$. Atoms that are not moving at all ($v = 0$) experience no force at all. As a result the atoms are slowed down. However, because there is no spatial confinement, the atoms are not trapped and they can drift away with small velocities. It should also be noted that not all atoms are slowed down. Only atoms that enter the interaction region within a certain velocity can be slowed to a standstill. Atoms moving too fast do not experience a force that is large enough to stop them before they leave the interaction region.

Electromagnetism

This chapter serves as a brief introduction into the topic of classical electromagnetism. In a first step, the theoretical foundation used to calculate the magnetic field generated by an arbitrary current density is derived. This formalism is later used to calculate the magnetic field generated the different sets of coils used in the experimental setup.

Classical electromagnetism can be described by a set of coupled partial differential equations known as *Maxwell's equations*:

$$\nabla \times \mathbf{E} = -\frac{\partial \mathbf{B}}{\partial t}, \quad (3.1)$$

$$\nabla \times \mathbf{B} = \mu_0 \mathbf{j} + \frac{1}{c^2} \frac{\partial \mathbf{E}}{\partial t}, \quad (3.2)$$

$$\nabla \cdot \mathbf{E} = \frac{\rho}{\epsilon_0}, \quad (3.3)$$

$$\nabla \cdot \mathbf{B} = 0, \quad (3.4)$$

with the electric field \mathbf{E} , the magnetic flux density \mathbf{B} , the current density \mathbf{j} , the charge density ρ , the vacuum permeability μ_0 , the vacuum permittivity ϵ_0 and the speed of light $c = 1/\sqrt{\mu_0\epsilon_0}$. Maxwell's equations can be interpreted in a following, simplified, way:

- A changing magnetic field induces an electric field (Eq. (3.1)).
- Any current density or change in electric field results in a magnetic field (Eq. (3.2)).
- Any electric charge is the source of an electric field (Eq. (3.3)).
- There are no magnetic charges, thus magnetic field lines are always closed loops (Eq. (3.4)).

3.1. Biot-Savart Law

To calculate the field generated by an arbitrary current density, for example a wire loop, a vector potential \mathbf{A} is introduced using the relation

$$\mathbf{B} = \nabla \times \mathbf{A}. \quad (3.5)$$

Using both Eq. (3.2) and Eq. (3.5) the vector potential \mathbf{A} can be calculated

$$\nabla \times (\nabla \times \mathbf{A}) = \mu_0 \cdot \mathbf{j} + \frac{1}{c^2} \frac{\partial \mathbf{E}}{\partial t}. \quad (3.6)$$

In static case, the time dependent part can be set to zero. Using, the *Coulomb gauge* ($\nabla \cdot \mathbf{A} = 0$)[Dem13] results in ¹

$$\Delta \mathbf{A} = -\mu_0 \cdot \mathbf{j}. \quad (3.7)$$

Solving this differential equation yields

$$\mathbf{A}(\mathbf{r}) = \frac{\mu_0}{4\pi} \int d^3\mathbf{r}' \frac{\mathbf{j}(\mathbf{r}')}{|\mathbf{r} - \mathbf{r}'|}. \quad (3.8)$$

With this equation it is now possible to calculate the vector potential at any position \mathbf{r} caused by any arbitrary current density $\mathbf{j}(\mathbf{r}')$. Equation(3.8) can also be expressed in terms of the magnetic flux density,

$$\mathbf{B}(\mathbf{r}) = \frac{\mu_0}{4\pi} \int d^3\mathbf{r}' \nabla \times \left(\frac{\mathbf{j}(\mathbf{r}')}{|\mathbf{r} - \mathbf{r}'|} \right). \quad (3.9)$$

This equation is known as the *Biot-Savart law* and will be used in the following section to calculate the field generated by a set of coils.

3.2. Helmholtz Coil

Many applications require a homogeneous magnetic field that extends over a large area. One possible option to generate such a field is using a Helmholtz coil. Such a coil is constructed using two identical coils with radius R placed at a distance l . The distance between the coils is set such that the generated field is homogeneous in the center. Using

¹ By making use of the Coulomb gauge ($\nabla \cdot \mathbf{A} = 0$); $\nabla \times (\nabla \times \mathbf{A}) = \nabla(\nabla \cdot \mathbf{A}) - \Delta \mathbf{A} = -\Delta \mathbf{A}$

Eq. (3.9) the flux density of such a coil is given by²,

$$\mathbf{B}_z(z) = \frac{\mu_0 NI}{2} \left(\frac{R^2}{(R^2 + (z - l/2)^2)^{3/2}} + \frac{R^2}{(R^2 + (z + l/2)^2)^{3/2}} \right) \mathbf{e}_z, \quad (3.10)$$

where μ_0 is the magnetic field constant, I is the current supplied to the coils and N is the number of turns per coil. The two terms in the bracket correspond to the two coils located at $z_0 = -l/2$ and $z_0 = l/2$ respectively.

In order to generate a homogeneous field, the gradient in the center has to vanish. Thus, Eq. (3.10) has to fulfill

$$\frac{d^2}{dz^2} \mathbf{B}(z)|_{z=0} = 0. \quad (3.11)$$

That this is the case if the coils are placed $l_{\text{helm}} = R$ apart from each other [Dem13]. The same derivation can be done for rectangular coils. Here the condition is fulfilled if

$$l_{\text{helm}} = 0.5445a, \quad (3.12)$$

where a is the side length of the rectangular coils [Hel55]. The field generated by such a rectangular Helmholtz coil is shown in Figure 3.1. The figure shows a large region of homogeneous magnetic field in the center. The magnetic field points only in \mathbf{z} -direction and is of constant amplitude. For such a configuration, there is a whole region of homogeneous field surrounding the center. This volume can be calculated to be [Hel55]

$$V_{\text{hom.}} = 1.018 \cdot 10^{-3} \cdot a^3. \quad (3.13)$$

In ultracold gas experiments such a coil configuration is often used to compensate external static magnetic fields such as earth's magnetic field or to generate the fields necessary to tune the Feshbach-resonances in ultracold atom systems [Chi+10].

3.2.1. Anti-Helmholtz coil

In ultracold quantum gas experiments it is often also required to apply well controlled magnetic field gradients. In order to generate gradient fields the polarity of one of the coils making up the Helmholtz pair is switched. The resulting configuration is called

² For simplicity this calculation is done for the magnetic flux density along the symmetry axis (\mathbf{B}_z) only.

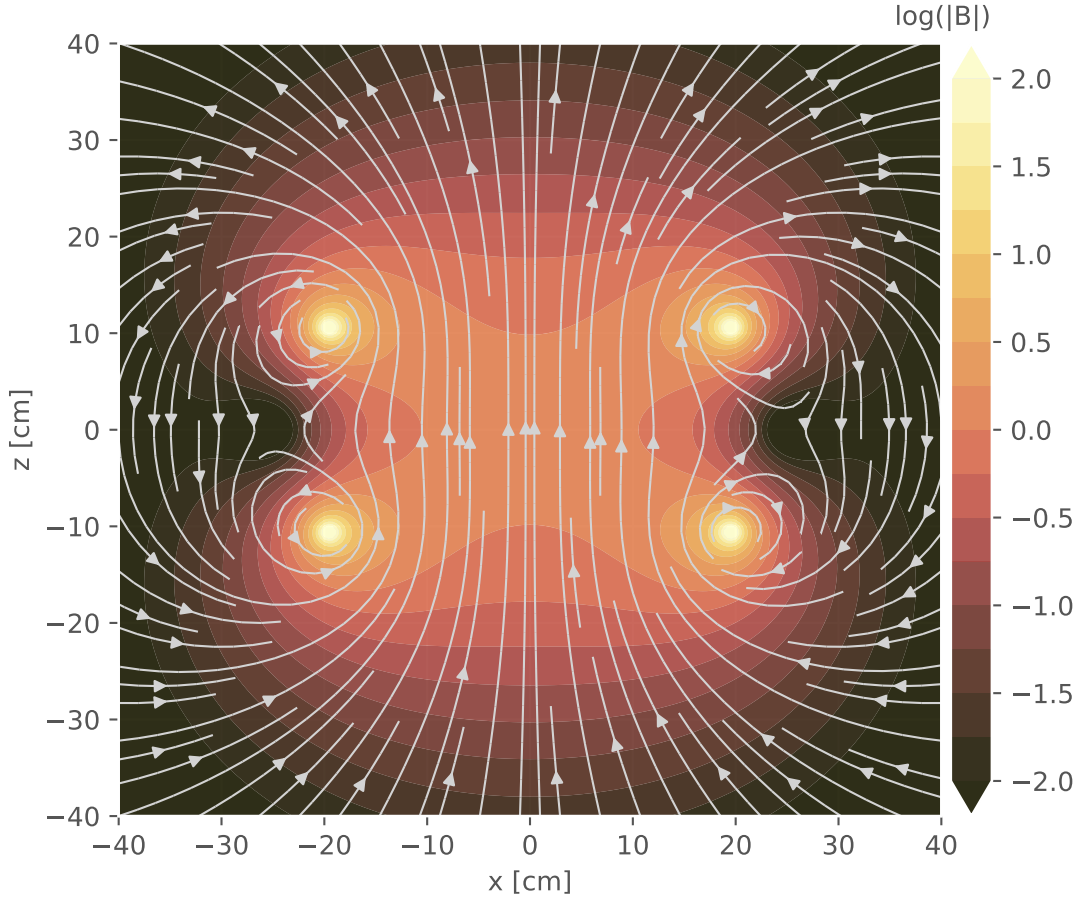


Figure 3.1.: Magnetic-field simulation of a Helmholtz coil. The coils lie in the x - y -plane and are centered around the origin. The plot shows a cut through $y = 0$. The coils are rectangular with a side length of $a = 39.0$ cm and are placed with a distance $l = 21.2$ cm apart from each other. Each coil has $N = 25$ turns and is supplied with a current of $I = 1$ A. The arrows indicate the field lines in the x - z -plane. The background shows the amplitude of the magnetic flux density on a logarithmic scale. A Helmholtz coil generates a field that is homogeneous around the center. This is indicated by the uniform amplitude in the center in combination with field lines that point only in the z -direction. The field is calculated using the code supplied in Appendix B.

anti-helmholtz. Using Eq. (3.9) the magnetic field of such a coil pair ³ can be calculated:

$$\mathbf{B}_z(z) = \frac{\mu_0 N I}{2} \left(\frac{R^2}{(R^2 + (z - l/2)^2)^{3/2}} - \frac{R^2}{(R^2 + (z + l/2)^2)^{3/2}} \right) \mathbf{e}_z. \quad (3.14)$$

³ Note that compared to Eq. (3.10) there is a minus sign accounting for the change in polarity of one of the coils.

In order to achieve a homogeneous field gradient the second and third derivative of the magnetic field have to vanish, thus fulfilling,

$$\frac{d^2}{dz^2}\mathbf{B}(z)|_{z=0} = 0 \quad \text{and} \quad \frac{d^3}{dz^3}\mathbf{B}(z)|_{z=0} = 0. \quad (3.15)$$

These conditions are fulfilled if the coils are placed

$$l_{\text{anti-helm}} = \sqrt{3} \cdot R \quad (3.16)$$

apart from each other [Dem13]. The field of such an Anti-Helmholtz coil is shown in Figure 3.2. Since this configuration is symmetric the fields generated by the two individual coils cancel each other in the center. The resulting field is a quadrupole field with gradients in both axial and in radial direction. This is illustrated by the field lines in Figure 3.2. Anti-Helmholtz coils can for example be used for the operation of magneto-optical traps (see Chapter 2.4.4).

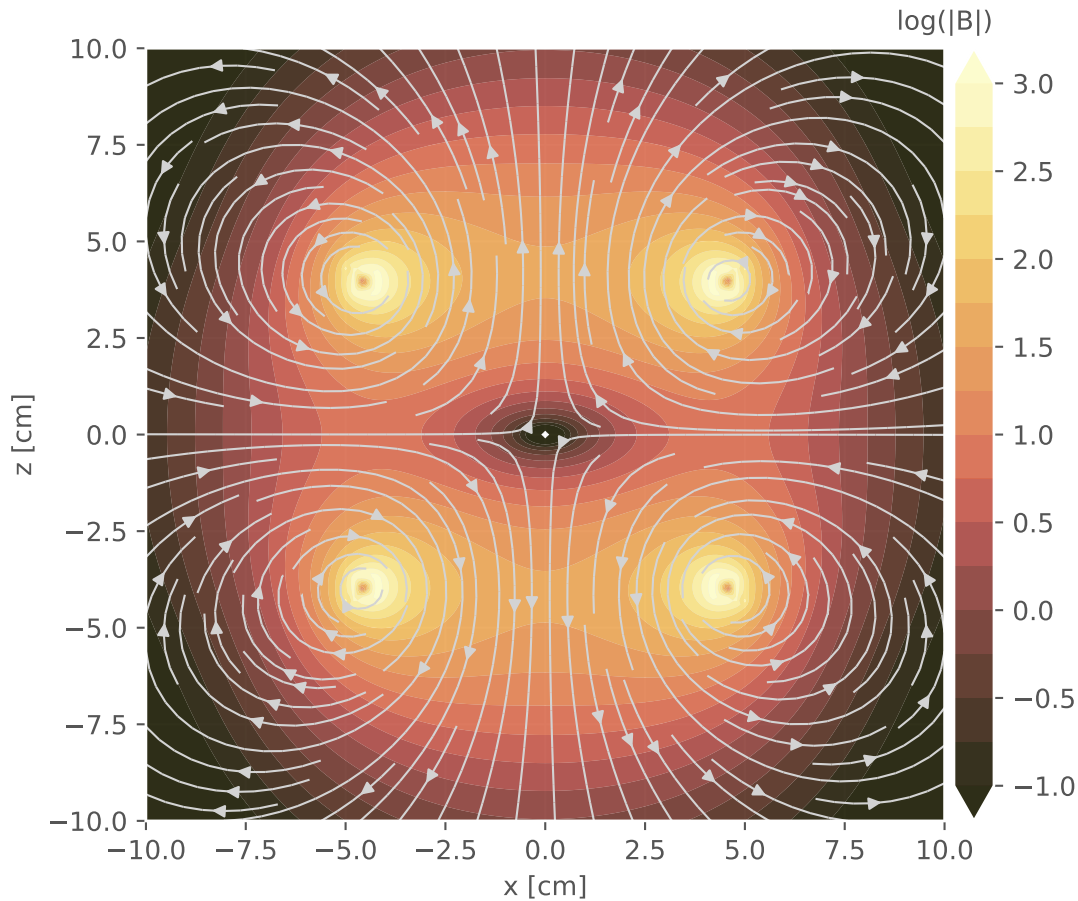


Figure 3.2.: Magnetic-field simulation of an Anti-Helmholtz coil. The coils lie in the x - y -plane and are centered around the origin. The plot shows a cut through $y = 0$. The coils are circular with a radius of $R = 4.25$ cm and are placed with a distance $l = 7.4$ cm apart from each other. Each coil has $N = 38$ turns and is supplied with a current of $I = 1$ A and $I = -1$ A respectively. The arrows indicate the field lines in the plane. The field generated by this kind of coil has a gradient in radial as well as in axial directions and is also known as a quadrupole field. The background shows the amplitude of the magnetic flux density on a logarithmic scale. The field is calculated using the code supplied in Appendix B.

Interferometry

Interferometry is a technique that uses the interference of two plane waves. Devices that make use of interferometry in order to extract information are called interferometers. Interferometers typically make use of electromagnetic waves but interferometers can also be realized using atoms [Mif+06] or electrons [MSS54]. Interferometers have a wide range of applications ranging from astronomy and optical metrology to precision manufacturing. In this chapter first the interference of two plane waves is discussed theoretically. The Michelson interferometer is introduced as an example of one of the experimental techniques of interferometry. It is derived how the changes in the interference pattern can be used in order to extract information regarding displacement and tip-/ tilt of an underlying system.

4.1. Interference of two Plane Waves

In the following discussion light is treated as a electric plane wave. Such a plane wave emitted from a coherent light source, e.g. a Laser, is given by

$$E(\mathbf{r}, t) = E_0 \cos(\omega t - \mathbf{k} \cdot \mathbf{r}) , \quad (4.1)$$

with the frequency of the light ω , the wave vector \mathbf{k} and position \mathbf{r} . The intensity $I \propto \mathbf{E}^2$ of two superimposed plane waves with the same amplitude E_0 and frequency ω is given by

$$I \propto E_0^2 \cdot [\cos(\omega t - \mathbf{k}_1 \cdot \mathbf{r}_1) + \cos(\omega t - \mathbf{k}_2 \cdot \mathbf{r}_2)]^2 , \quad (4.2)$$

where the subscript denotes the wave vector and position of two individual plane waves. In the case of visible light, the electric field is oscillating on the order of femto seconds (10^{-15} s). A detector, for example a photodiode, time-averages over many periods of the electromagnetic wave. The time average of Eq. (4.2) reads [Dem13]

$$\bar{I} \propto E_0^2 \cdot [1 + \cos(\Delta\varphi(\mathbf{k}_1, \mathbf{k}_2, \mathbf{r}_1, \mathbf{r}_2))] , \quad (4.3)$$

with the phase difference $\Delta\varphi = \mathbf{k}_1 \cdot \mathbf{r}_1 - \mathbf{k}_2 \cdot \mathbf{r}_2$. Depending on the phase difference the intensity can vary between $I = 0$ and $I = 2E_0^2$ and as the cosine has a periodicity of 2π , a repeating pattern can be observed¹. Thus, when superimposing two plane waves the resulting wave can be of greater, lower or the same amplitude. This phenomenon is called interference and the resulting pattern is known as an interference pattern.

4.2. Michelson Interferometer

An interferometer is a device that uses interference in order to extract informations such as displacement and orientation. There are different kinds of interferometers, each designed for a specific use case. In this section the Michelson interferometer is introduced. It is derived how this kind of interferometer can be used in order to gain insights on the tilt and displacement of an underlying system. A schematic setup of a Michelson interferometer is shown in Figure 4.1. The interferometer is constructed using a beamsplitter that splits the light into two individual arms. At the end of each arm a mirror acts as a retroreflector, sending the light back. The two reflected beams are superimposed on a detector where the interference pattern can be recorded. In this thesis, a Michelson interferometer is used in order to characterize the stability of a manual positioning stage used for placing a diffraction-limited objective.

In general the two plane waves are not perfectly aligned. In the following, one of the waves is slightly tilted with respect to the other wave. In such a configuration the two wave- and position vectors of the co-propagating plane waves are

$$k_1 = \frac{2\pi}{\lambda} \begin{pmatrix} \sin(\alpha) \\ \cos(\alpha) \cos(\beta) \\ \sin(\beta) \end{pmatrix}, k_2 = \frac{2\pi}{\lambda} \begin{pmatrix} 0 \\ 1 \\ 0 \end{pmatrix} \quad \text{and} \quad r_i = \lambda \begin{pmatrix} x_d \\ d_i \\ z_d \end{pmatrix}, \quad (4.4)$$

with the tilt angles α and β , the position on the detector x_d and z_d and the distance of propagation of the two plane waves d_i , $i \in [1, 2]$. The resulting phase difference is given by

$$\Delta\varphi = \frac{2\pi}{\lambda} \left[\underbrace{(\sin(\alpha \cdot x_d) + \sin(\beta \cdot z_d))}_{\varphi(x_d, z_d)} + \underbrace{(\cos(\alpha) \cos(\beta) d_1 - d_2)}_{\varphi_0} \right], \quad (4.5)$$

¹ This is only the case if the light is treated as a plane wave. In general this is not the case and the description of a Gaussian beam has to be used. In this case, the interference pattern observed for co-propagating beams is that of concentric rings.

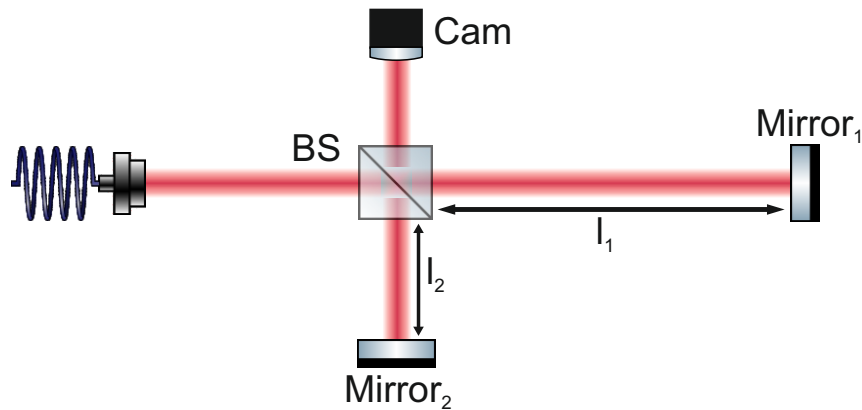


Figure 4.1.: Schematic setup of a Michelson interferometer. The coherent beam is split into two individual arms by a beam splitter (BS). At the end of each arm, a mirror is used to retroreflect the light. Both reflected beams are superimposed on a detector (CAM). The detector can either be a photodiode or a camera depending on the application. If a camera is used, an interference pattern can be observed. The interference pattern changes depending on the path difference $\Delta d \propto l_1 - l_2$ and the orientation of the two mirrors with respect to each other. In a general case where the two mirrors have a slight misalignment a stripe pattern is observed on the camera. Changes in the interference pattern can be used in order to calculate the changes in path difference and alignment of the mirrors.

with a phase $\varphi(x_d, z_d)$ that depends on the position on the detector and a phase offset φ_0 that depends on the tilt and path difference. The resulting interference pattern on the detector can now be calculated by substituting Eq. (4.5) into Eq. (4.3). Different configurations for the tilt angles and path difference create different patterns, some of which are depicted in Figure 4.2. In the case where the plane wave is only tilted with respect to one axis the pattern has either horizontal or vertical stripes, depending on the tilt axis (see Figure 4.2 a) and b)). The periodicity of the striped pattern depends on the tilt angle. In a general case where the wave is tilted with respect to both axes, the resulting stripe pattern has an angle that depends on the ratio between the two different angles (Figure 4.2 d). When the path difference changes, the pattern is shifted as a whole while the tilt remains constant (compare Figure 4.2 a) and c). The interference pattern is highly sensitive to changes in the tilt angles and path difference. This allows for precise measurement of an underlying system. For example, if the position of one of the mirrors changes, so does the path difference. This immediately shows up in the interference pattern as a global phase shift. If the angle of one of the mirrors changes, this shows up as a change in the angle and periodicity of the stripe pattern. There are many applications in which a Michelson interferometer can be used. One prominent example is the *Laser*

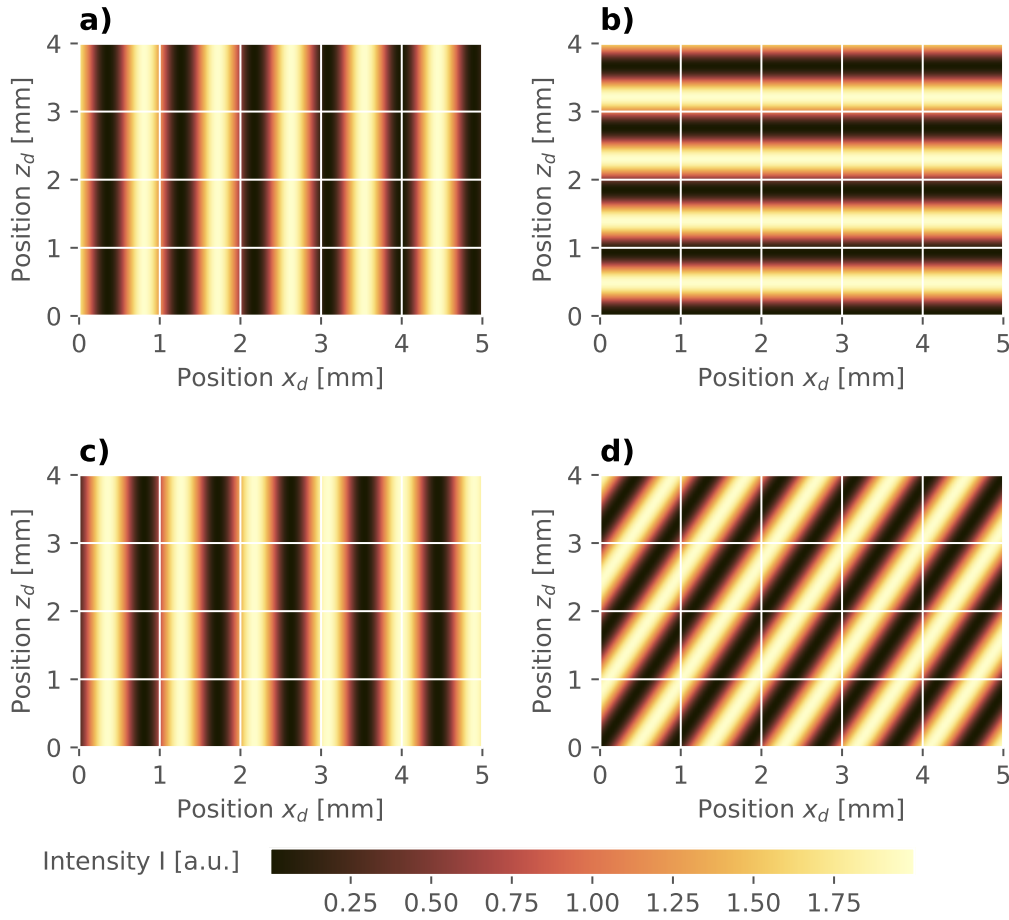


Figure 4.2.: Different interference patterns observed using a Michelson interferometer reveal information on displacement and tilt angles. The patterns are shown as they would appear on a detector (e.g. a camera). They are calculated by substituting Eq. (4.5) into Eq. (4.3). In a) one of the mirrors of the interferometer is tilted by a small angle α with respect to the y -axis and $\beta = 0$. The corresponding interference pattern varies along the x -axis of the detector, creating a horizontal stripe pattern. In b) the mirror is tilted by a small angle β with respect to the x -axis and $\alpha = 0$. The resulting pattern varies along the z -axis of the detector. A vertical stripe pattern can be observed. In c) the mirror has the same tilt as the one in a). The length of one of the arms is changed resulting in a change of optical path length. Compared to a), the pattern is shifted as a whole along the x -axis of the detector. In d) the mirror is tilted with respect to both axes. This results in an angled stripe pattern where the angle depends on the ratio between α and β . In all cases the periodicity of the stripe pattern depends on the magnitude of the tilt angle.

Interferometer Gravitational-Wave Observatory (LIGO), where a Michelson interferometer is used to measure displacements smaller than the proton diameter ($\sim 10^{-15}$ m) over a distance of 4 km [Zuc07].

Experimental Apparatus

An overview of the apparatus is depicted in Figure 5.1. The experimental apparatus operates much like the setup that is currently being used in the Dipolar Quantum Gases Group at the PI5 where the details are thoroughly described in [Mai15]. Solid dysprosium is heated in the effusion cell. The effusion cell is typically operated at a temperature of $T = 1100^\circ\text{C}$. At these temperatures a hot atomic beam with a forward velocity of $v_{\text{mean}} \approx 430 \text{ m/s}$ exits the oven. The atoms are first transversely cooled by the 2D optical-molasses section and afterwards slowed down longitudinally by a Zeeman slower¹. In the Zeeman slower, the longitudinal velocity of the atoms is reduced to $v < 8 \text{ m/s}$. These slowed down atoms are trapped in a magneto-optical trap. Here, their temperature is reduced below $T < 500 \mu\text{K}$. This cloud of trapped, cold atoms is then transferred to optical traps where further cooling is done in order to reach quantum degeneracy ($T < 100 \text{ nK}$). In the case of the bosonic isotopes of dysprosium, the result is a Bose-Einstein condensate (BEC). When using the fermionic isotopes a degenerate fermi gas is produced. Unlike the previous apparatus, the new machine can not only perform experiments with quantum degenerate gases trapped in harmonic traps but also load atoms into optical lattices. Here, single-site resolution imaging enables the studies of site- and spin correlations. In such a *quantum-gas microscope* phenomenon ranging from quantum magnetism to lattice spin models can be studied [CI17].

In the scope of this thesis some of the components that are used in the experimental apparatus were set up and characterized. These components will be discussed in more detail in the following sections.

¹ Details regarding the Zeeman slower are describes in [Klu19].

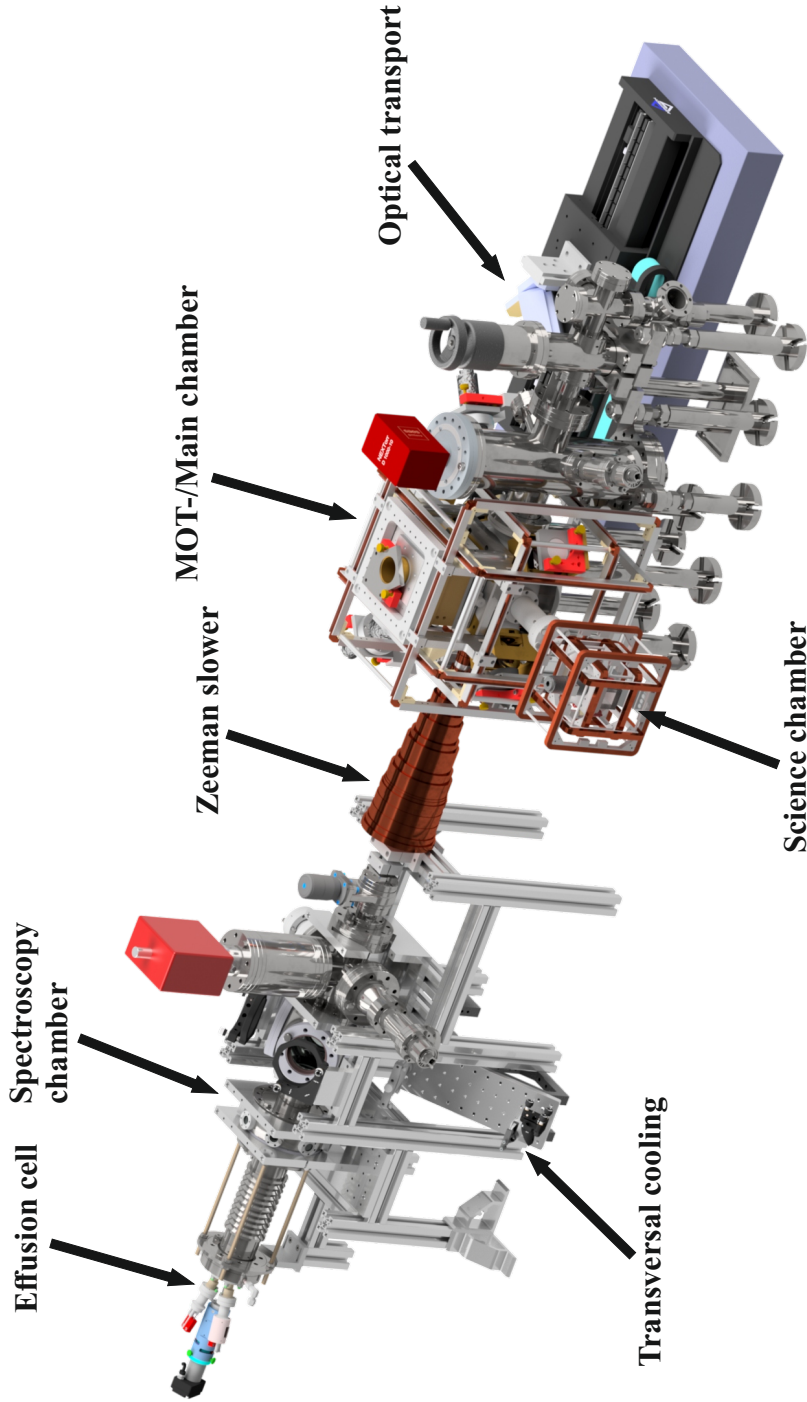


Figure 5.1.: Overview of the whole experimental setup. A atomic beam of dysprosium is produced in the effusion cell. Here, solid dysprosium is heated to $T = 1100\text{ }^\circ\text{C}$. The spectroscopy chamber is used to monitor the output of the effusion cell. In this thesis, the spectroscopy chamber is used in order to characterize the atomic beam. The transversal cooling section makes use of a two-dimensional optical molasses in order to reduce the transversal velocity of the atomic beam. A Zeeman slower is used to slow the longitudinal velocity of the atomic beam to $v \lesssim 8\text{ m/s}$. In the MOT-/Main chamber, the slowed down atoms are captured in a magneto-optical trap (MOT). In the MOT, the atoms are cooled down further to $T < 500\text{ }\mu\text{K}$. The cloud of trapped, cold atoms is then transferred to optical traps where further cooling is done in order to reach quantum degeneracy ($T < 100\text{ nK}$). This ultracold cloud of atoms is then optically transported to the science chamber where they are loaded into the UV optical lattice.

5.1. Magnetic Field Control

Magnetic atoms such as dysprosium are extremely sensitive to external magnetic fields. Therefore, when performing dipolar quantum gas experiments magnetic-field control plays an important role. In the experimental apparatus, many different coils are used in order to generate precise magnetic fields and magnetic field gradients. In order to design the coils, the magnetic field was first calculated theoretically. A detailed description on how the magnetic field calculations are done is given in Appendix B.

5.1.1. Compensation Coils

The predominant external magnetic field that has to be considered is Earth's magnetic field. The field is constant and at the position of the experiment the magnetic field strength is $|B_{\text{earth}}| \approx 500$ mG. As there are also large coils producing large magnetic fields, magnetic materials that are nearby can be magnetized thus generating stray fields with varying amplitude and pointing. Additionally large currents can cause stray fields that need compensation. In order to compensate these external magnetic fields, three pairs of coils are installed surrounding the main chamber of the experiment (see Figure 5.1). The individual coil pairs are arranged in a Helmholtz configuration. This is done in order to maximize the region of homogeneous field in the center in order to avoid introducing new gradients to the system. Each coil has 25 windings in a 5x5-pattern and is wound using litz-wire². Additionally every coil has three layers of a 0.2 mm by 10 mm copper band that form a separate loop. This is done in order to allow for the generation of small offset fields independent of the main coil. Also, the copper-band can be used in an anti-Helmholtz configuration in order to compensate small gradients that may exist. The dimensions of the different coil-pairs are listed in Table 5.1. As there are physical constraints on the placement of the coils, the side lengths a and distances l were optimized to be as close to the ideal situation of $l/a = 0.5445$ as possible (see Chapter 3.2). Additionally, the Z-coil could only fit in the experiment by including a bend around one of the vacuum-parts. Simulations of the generated field confirmed that this deviation from a rectangular configuration can be neglected³.

The field generated by the compensation coils is shown in Figure 5.2. The field is calculated using the code provided in Appendix B. In the simulation the bend of the z-coil is not

² The litz wire used in this experiment consists of 270 isolated wires with a diameter of 0.1 mm that are bundled together into a one thicker wire. This is beneficial for fast switching and high frequency applications as thin wires are less affected by the skin effect.

³ The simulations were performed by Kevin Ng using finite-element simulations in COMSOL.

considered. The figure shows that the homogeneity of the three different field directions not perfectly consistent. This is due to the fact that the three different coil pairs deviate from the ideal Helmholtz condition by varying amounts. Nevertheless, all coils generate fields with a homogeneity that is sufficient for the experiments that are planned. It should also be noted that these are simulations of the field in an ideal case. In the experiment the placement of the individual coils is precise on the order of millimeters. Also as the coils surround a stainless-steel vacuum chamber, deviations of the magnetic field are expected due to the magnetization of the steel components⁴.

Table 5.1.: Summary of the specifications of the compensation coils. The side lengths and distances refer to the minimum measurement. For an ideal square Helmholtz configuration, $d/a = 0.5445$. Each coil has 25 turns of 2.1 mm^2 cross-section litz wire. Additionally each coil has three turns of a copper band that are wound as a separate loop. The field generated by the litz-wire in the center is listed in the respective axis (i.e. B_x for X-coils etc.). The field generated by the copper band is $B_i \approx 120 \text{ mG/A}$ for all axis.

| | side length a [mm] | distance l [mm] | l/a | field in the center [G/A] |
|---------|----------------------|-------------------|-------|---------------------------|
| X-Coils | 404 | 224 | 0.554 | 1.04 |
| Y-Coils | 390 | 212 | 0.544 | 1.05 |
| Z-Coils | 374 | 204 | 0.545 | 1.09 |

⁴ However, this effect is minimized by using low magnetic permeability materials where $\mu - 1 \ll 1$. In the case of this experiment, components are made of 316L, 316LN and 316LN ESR stainless steel.

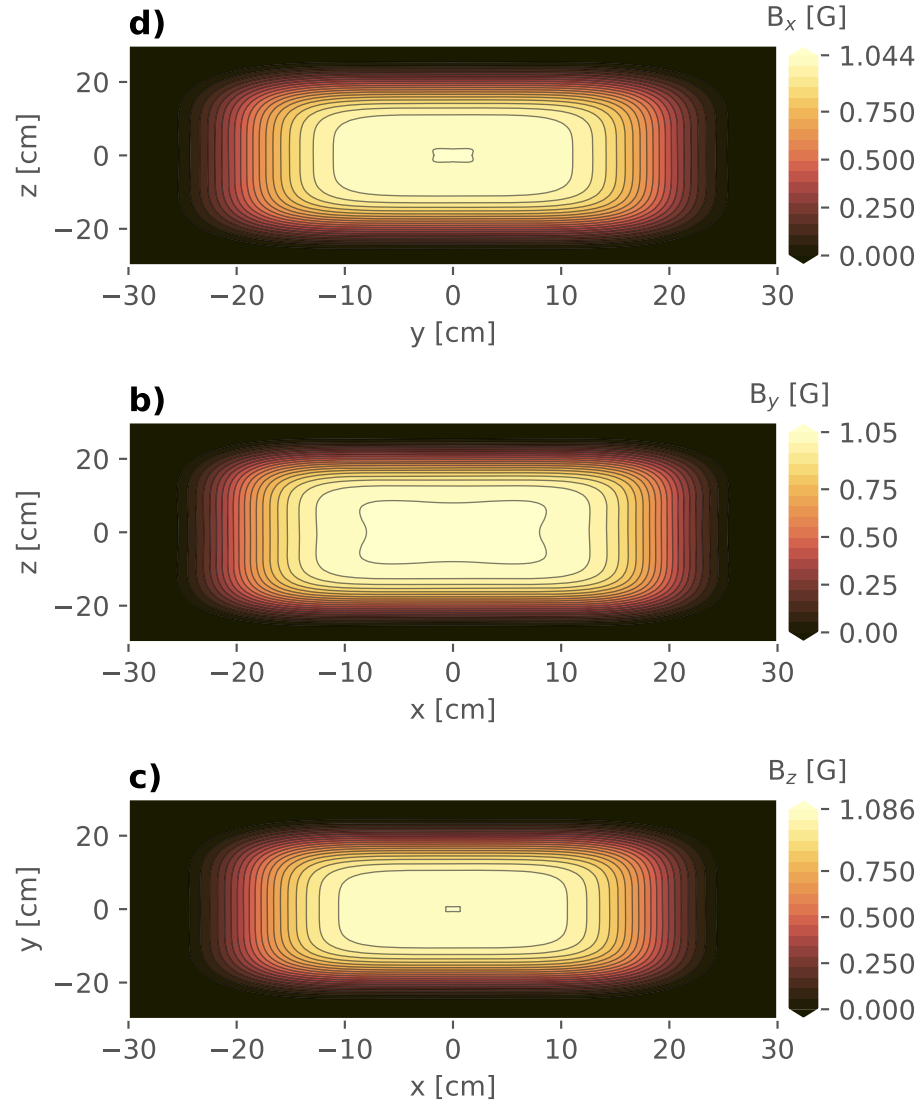


Figure 5.2.: Simulated field generated by the compensation coils. The compensation coils consist of three individual Helmholtz pairs. The three pairs are placed orthogonal with respect to each other. This way, each coil is set up to provide a magnetic field in either x-, y-, or z-direction while their contribution in the other two directions is minimized. The coils are rectangular with a side length on the order of $a \sim 400$ mm. Their exact specifications are summarized in Table 5.1. In this example, each coil is supplied with a current of $I = 1$ A. The figures show the total field generated by all coils. The different sub figures a), b) and c) show the different magnetic field components B_x , B_y and B_z , respectively. For simplicity the field is only depicted in certain plane. The amplitude of the magnetic field in the center is $B_i \sim 1$ G/A for all three directions.

5.1.2. Gradient-/ and Feshbach Coils

For experiments in the main chamber the magnetic field amplitude as well as the gradient has to be controlled. For the operation of the MOT a magnetic field gradient has to be applied in both the axial and radial direction. This is done with a single pair of *gradient coils* in an anti-Helmholtz configuration. As was discussed previously in Chapter 3.2 such a coil pair is able to generate a quadrupole field providing the magnetic field gradients that are needed. A magnetic field gradient may also be applied for levitation of the quantum gas, offsetting the force applied by gravity [Sch17].

For many of the experiments performed in optical traps a homogeneous magnetic field has to be applied. This is done in order to change the scattering length a in order to tune the interactions in the system. The scattering length can be changed by so called Feshbach resonances and can be tuned by varying the magnetic field strength. Because of this, the coils used for tuning the scattering length are often referred to as *Feshbach coils*. Both the gradient- and Feshbach coil are placed directly outside the chamber. The coils are epoxied to a brass support structure using Electrolube TCOR75S. The whole assembly is inserted into the recessed viewport of the main chamber and secured using titanium screws. The assembly containing both the gradient- and Feshbach coils in its assembled form is depicted in Figure 5.3. Due to the tight tolerances, winding these coils was a challenging task and the whole procedure is described in Appendix A.

Gradient Coils

For the gradient coils two circular coils in an anti-Helmholtz configuration are used. The specifications of the gradient coils is summarized in Table 5.2. The simulated magnetic field generated by the gradient coils is shown in Figure 5.4. Because of the symmetry of the system, the field generated in x- and y-direction is the same. For simplicity only the field in x-direction (B_x) is shown. Figure 5.4 a) and b) show the field amplitude of B_x and B_z , respectively. Because of the anti-Helmholtz configuration the field in the center is $B_x = B_z = 0$. Moving away from the center, the field changes rapidly. This behaviour becomes more visible in Figure 5.4 c) and d). The figures show the magnetic field along the x- and z-axis for B_x and B_z , respectively. Around the center the field changes linearly. Thus, the magnetic-field gradient in the center is nearly flat. In Figure 5.4 e) and f) the gradient around a small region around the center is shown. The gradient is sufficiently flat for all experiments that are going to take place in the main chamber.

When operating a MOT, the trapping potential V proportional to the magnetic field

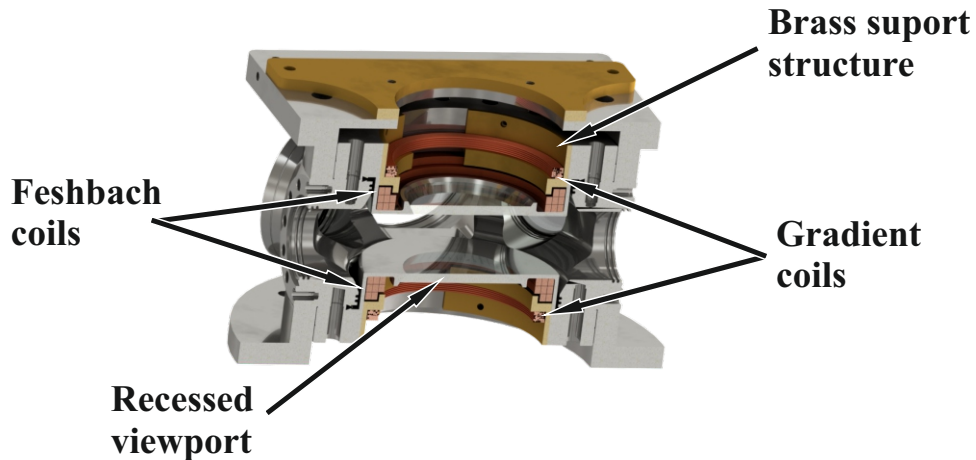


Figure 5.3.: Overview of the MOT-/Main chamber. In order to achieve the high-resolution needed to image small structures like self-bound droplets [Sch+16] or exotic patterns [Her+21] the objective has to be placed close to the atoms. This is achieved using a vacuum chamber with recessed viewports. These recessed viewports not only allow for good optical access but can also be used to place coils close to the atoms resulting in large magnetic field and magnetic field gradients. The gradient- and Feshbach coils are epoxied to a brass support structure. This support structure is inserted into the recessed viewports of the main chamber and secured using titanium screws. The Feshbach coils are arranged in nearly Helmholtz configuration while the gradient coils are arranged close to anti-Helmholtz configuration.

gradient,

$$V \propto \sqrt{\nabla B}. \quad (5.1)$$

Thus, the confinement of the atoms in z-direction (axial direction) is stronger than in the x-direction (radial direction). As a result of this, the MOT is not spherical but rather an oblate spheroid that is compressed in z-direction. This is to be expected when operating a MOT with a single anti-Helmholtz coil.

Table 5.2.: Summary of the specifications of the gradient coils. They consist of two circular coils with dimensions listed below. The dimensions refer to the minimum radius and distance. The coils are designed to be close to the ideal anti-Helmholtz condition of $l/r = \sqrt{3}$. Each coil has 38 turns of a wire with 1 mm diameter.

| radius r [mm] | distance l [mm] | l/r | $\nabla B_{x/y}$ [(G/cm)/A] | ∇B_z [(G/cm)/A] |
|-----------------|-------------------|-------|-----------------------------|-------------------------|
| 42.5 | 74.0 | 1.74 | 0.74 | 1.49 |

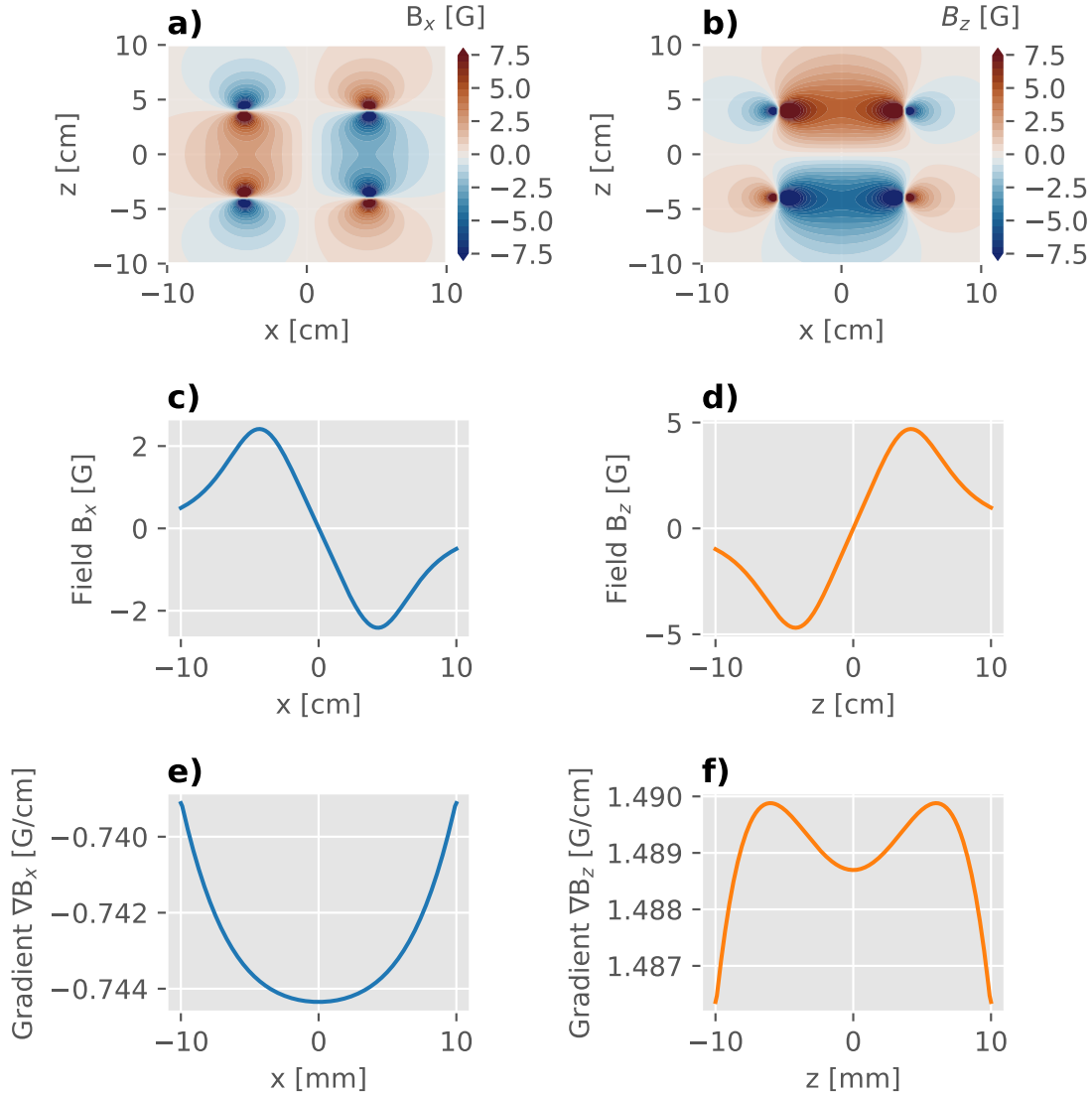


Figure 5.4.: Magnetic field generated by the gradient coils. The coils are constructed using an anti-Helmholtz pair of circular coils. The coils have a inner radius of $r = 42.5$ mm and are placed $l = 74.0$ mm apart from each other. Each coil is wound using 38 turns of a 1 mm-diameter wire. Figures a) and b) show the magnetic field in B_x and B_z , respectively where the z -axis is the symmetry axis of the coil pair. For simplicity only B_x and B_z are shown. The behavior of B_y is analogous to that of B_x . Because of the symmetry of the system, the amplitude of the field in the center is $B_i = 0$. This is highlighted in figures c) and d). Here, cuts of the magnetic field along the x - and z -axis are shown. Moving away from the center the amplitude of the field changes nearly linearly. In figures e) and f) the gradient of the B_x and B_z is shown. The gradients for B_x and B_z are shown in c) and d). As a result of the nearly linearly changing amplitude of the field around the center, the gradient is nearly constant. It should be noted that the sign and magnitude of the gradient is different for B_x and B_z . This is important for the operation of a MOT as the sign of the gradient determines the polarization of the light. Also because the gradient in z -direction is stronger, the trapping potential is not a sphere but rather an oblate spheroid that is compressed in z -direction.

Feshbach Coils

In order to generate a homogeneous magnetic field around the center region, the Feshbach coils are constructed using two circular coils in an Helmholtz configuration. They are designed to operate at large currents of up to $A_{\max} \sim 50$ A. In order to allow for these large currents, the coils are constructed using a 4.3 mm by 3.3 mm hollow wire. Thus allowing for water to flow through the wire acting as a coolant. The specifications of the Feshbach coils are listed in Table 5.3. The simulated magnetic field generated by this set of coils is shown in Figure 5.5. The figure shows the magnetic field in two different directions B_x and B_z . Because of the symmetry of the coils, the magnetic field in x-direction and in y-direction behaves the same and for simplicity only B_x is shown. The coils are designed to generate a homogeneous magnetic field in z-direction. Figure 5.5 a) and b) show that the off-axis fields are negligible around the center, $B_x < 100 \mu\text{G}$. The field generated in z-direction is large, $B_z \sim 1.5$ G. For the field in z-direction a cut along the x-/ and z-axis is shown in Figure 5.5 c). As is expected for a Helmholtz coil, B_z is flat around the center region. In order to quantify this behavior, the gradient ∇B_z is calculated along the two axis and depicted in Figure 5.5 d). In a volume of $V \sim (10 \text{ mm})^3$ the magnetic field has a small gradient only, $\nabla B_z < 0.01$ G/cm. This is sufficiently flat for the experiments that are planned to take place in the main chamber. If smaller gradients are required, the compensation coils described above can also be used in order to apply small gradients that can be used to compensate the residual gradient of the Feshbach coils.

Table 5.3.: Summary of the specifications of the Feshbach coils. They consist of two circular coils with dimensions listed below. The dimensions refer to the minimum radius and distance. The coils are designed to close to the ideal Helmholtz condition of $l/r = 0.5$. Each coil has eight turns of wire. Because the coils are designed to operate at large current, a 4.3 mm by 3.3 mm hollow copper wire is used. Thus, the wire also functions as piping for the cooling water.

| radius r [mm] | distance l [mm] | l/r | B_z [(G/A)] | ∇B_z [(G/cm)/A] |
|-----------------|-------------------|-------|---------------|-------------------------|
| 40.8 | 38.0 | 0.47 | 1.509 | < 0.01 |

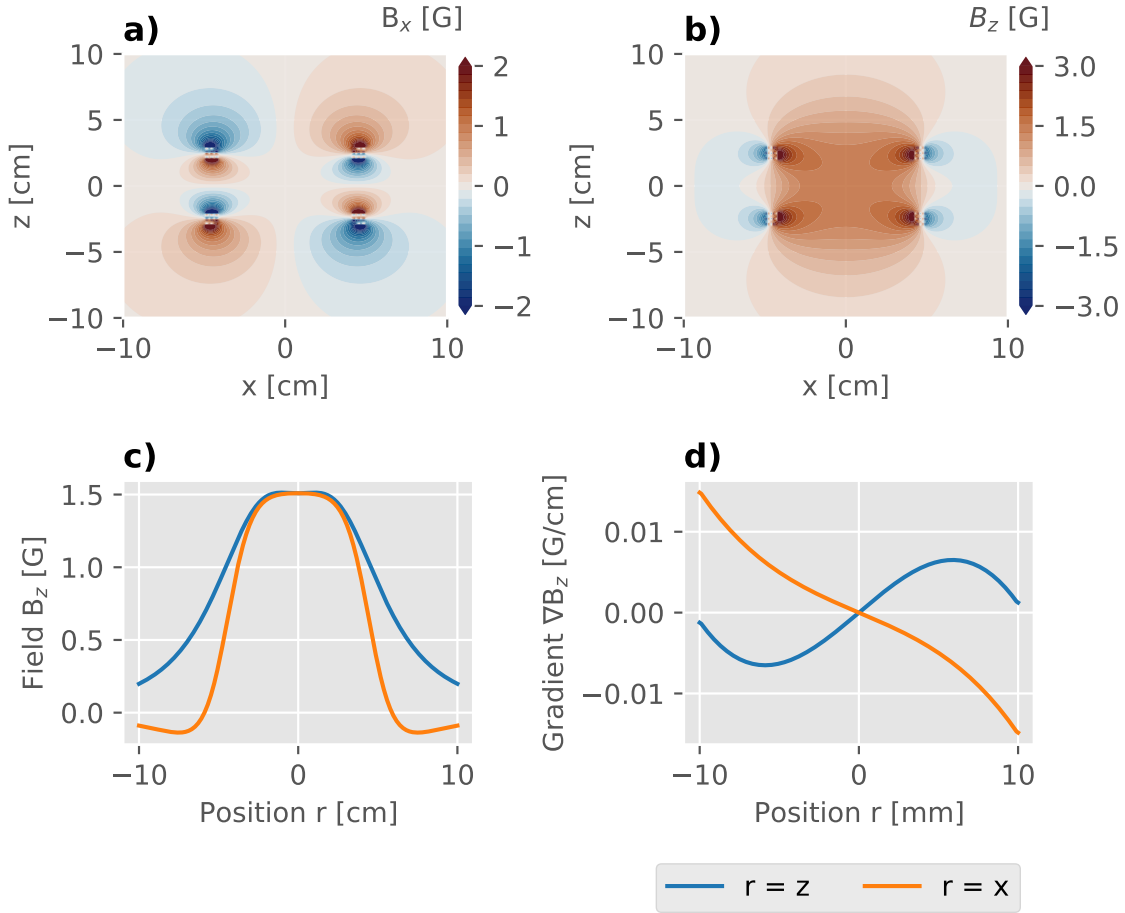


Figure 5.5.: Magnetic field generated by the Feshbach coils. The coils are constructed using a Helmholtz-pair of circular coils. The inner radius of the coils is $r = 40.8$ mm. The two coils are placed $l = 38.0$ mm apart from each other. Figures a) and b) show the magnetic field in B_x and B_z , respectively. Because the coil is designed to be close to the Helmholtz condition, in the center the magnetic field vector only has one component. Thus, in the center $B_z \approx 1.5$ G while $B_x = B_y < 100\mu$ G. Also, B_z is flat around the center. This is also highlighted in Figures c) and d). Figure c) shows cuts of B_z along the x -/ and z -direction. Around the center, the amplitude is nearly flat. To quantify this, the gradient is calculated along the two different axis and shown in Figure d). Around the center region the gradient is close to zero ($\nabla B_z < 0.01$ G/cm). This is sufficiently flat for the experiments that are planned to take place in the main chamber. Note that individual wires are visible in the simulation because they are modeled as thin wires while their real size is on the order of 4 mm.

5.2. Manual Positioning Stage

The structures that can be observed in an ultracold dipolar quantum gas are on the order of $10\ \mu\text{m}$ [Mai15]. Self-bound droplets can be as small as $\sim 300\ \text{nm}$ [Sch+16]. In order to resolve these structures a custom high-resolution imaging system is needed. The imaging system consists of a microscope objective with a numerical aperture of $NA = 0.5$ and is diffraction limited. The resolution of the imaging system

$$r = \frac{1.22\lambda}{2NA}, \quad (5.2)$$

shows that features as small as $r \approx 513\ \text{nm}$ can be observed when using blue light at $\lambda = 421\ \text{nm}$.

In order to reach this kind of resolution the objective itself has to be positioned with high accuracy. This is achieved by using a combination of different positioning stages. Manual positioning stages are used for the coarse positioning. A three-axis piezo stage with a travel range of $300\ \mu\text{m}$ is used to position the objective with a resolution on the order of nanometers⁵. The whole assembly is shown in Figure 5.6. In the scope of this thesis the coarse positioning stage was designed and characterized.

5.2.1. Characterization of the Z-Stage

The z -stage is a custom design that was manufactured by the in-house workshop. It is constructed using exclusively non-magnetic materials. The main body is brass and the ceramic linear bearings are made of zirconium oxide. As the resolution is expected to be on the order of $10\ \mu\text{m}$, a Michelson interferometer is used in order to characterize the positioning stage. Even simple interferometric techniques allow for measurements on the order of $1\ \text{nm}$ and thus allow for precise characterization of the mechanical properties. For the measurements the mirror of one of the arms of a Michelson interferometer is placed on top of the manual positioning stage. By moving the stage, the mirror position also changes and the interference pattern is recorded on a camera⁶. As described in Chapter 4.2 the interference pattern can be used in order to precisely measure on the displacement and tilt of the mirrors.

An initial test of the setup is shown in Figure 5.7. Here, the micrometer screw used to adjust the height of the positioning stage is turned by half a turn, lowering the stage. The interference pattern depicted in Figure 5.7 a) is recorded before turning the screw. The

⁵ The piezo stage used is a P-562, three-axis nanopositioning stage from Physik Instrumente

⁶ The camera used is a Logitech Webcam Pro 9000.

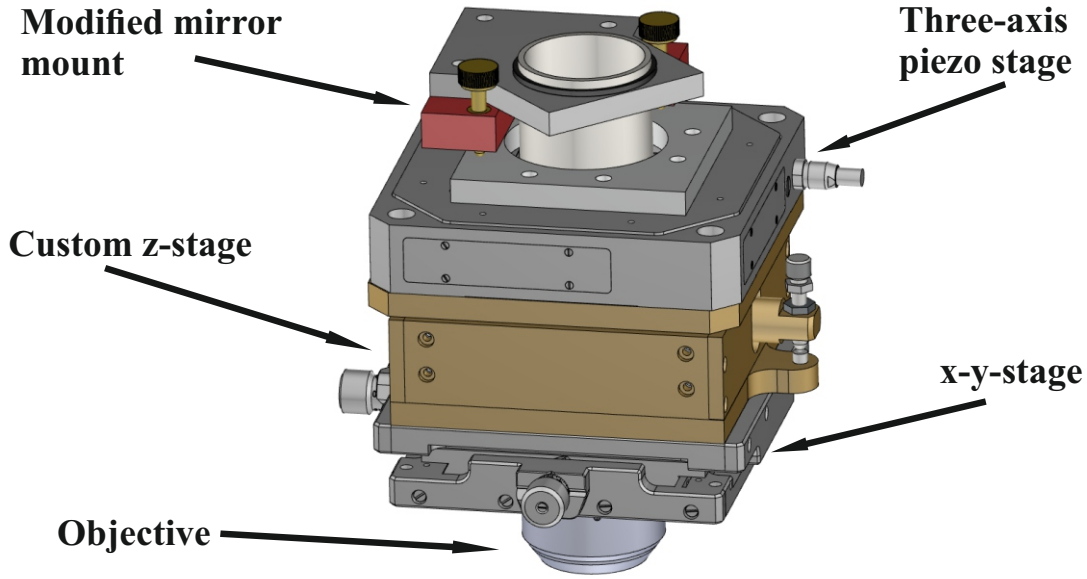


Figure 5.6.: Overview of the stack of positioning stages used for the positioning of the diffraction limited objective. The coarse positioning is done by a manual x - y -stage (Owis, KT 150-D80-UM) and a custom z -stage manufactured by the in-house workshop. Together, these two stages allow for positioning with a large travel range of $d = \pm 5$ mm in all three directions with a resolution of $r < 10$ μm . A custom mirror mount (Radiant Dyes, MXI-2-3027 modified) is used for tip and tilt adjustment. A three-axis piezo stage with a travel range of $d = 300$ μm is used to position the objective with a resolution on the order of nanometers. The objective is fixed to the mirror mount and supported by a titanium tube.

one shown in b) is recorded afterwards. A clear change in the interference pattern can be observed. This indicates that the tilt of the mirror changed between the two shots. Figure 5.7 c) and d) show two interference patterns that are calculated using Eq. (4.3) and Eq. (4.5). In the calculations the angles α and β and the path difference $d_1 - d_2$ are set such that the resulting interference pattern replicates the one measured in the experiment. From the calculated interference patterns the change in α and β can be deduced. In the example depicted in Figure 5.7, the change of the angles is $\Delta\alpha = 1.0(5)$ mrad and $\Delta\beta = 0.20(4)$ mrad. Note that in this example the stage is moved down. When moving the stage up (i.e. turning the micrometer screw the other way) the absolute change of α and β is reduced. This is due to the way the stage is constructed. The design uses one micrometer screw that pushed against the bottom plate of the mount in order to move the stage up. Also two springs are used in order to stabilize the stage and reduce the load on the linear bearings and the screw. Because of the one screw design, the force that lifts up the stage is applied on one side only. As a result, the stage can tilt in accordance to the mechanical tolerances of the system. Pushing the stage up against the springs seems

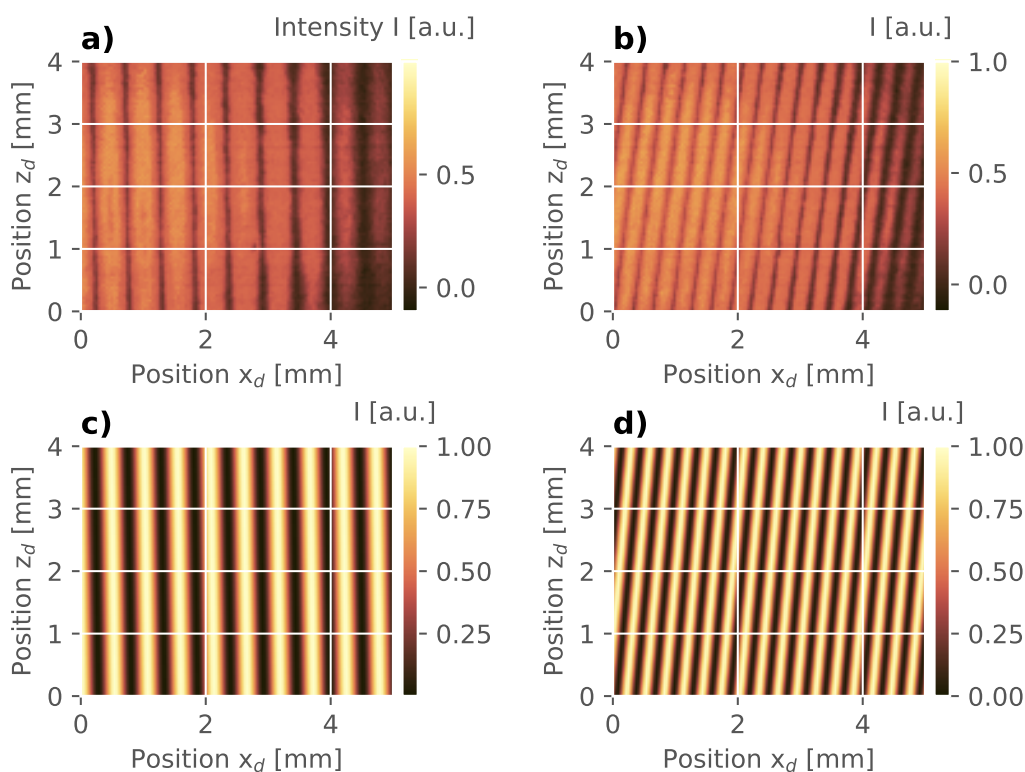


Figure 5.7.: Different interference patterns that are observed on a Michelson interferometer. The mirror of one of the arms of the interferometer is mounted to the z -stage. That way, if the stage is adjusted, changes in the position of the mirror can be detected as a change in the interference pattern. In Figures a) and b) the experimental data is depicted. Between the two images the micrometer screw used to adjust the height of the stage is turned by half a turn, lowering the stage. The interference pattern changes not only in the stripe spacing but also in the angle of the stripe pattern between the two images. The change in interference pattern indicates that the angle of the mirror changed while adjusting the height of the stage. Figures c) and d) show two interference patterns that are calculated using Eq. (4.3) and Eq. (4.5). The parameters are set such that they replicate the experimental data.

to lead to a more stable situation. It should also be noted that the tilt of the stage only happens once when moving either up or down. If the stage is raised continuously the change in the angles that occur after the initial change is reduced to < 0.1 mrad.

Travel Range

The micrometer screw used to raise or lower the z -stage has a pitch of $p = 350 \mu\text{m}$. As there is a one-to-one correspondence, for one turn of the micrometer screw the stage should move up or down by a distance $d = 350 \mu\text{m}$. As was discussed in Chapter 4.2, a change in path difference results in an overall shift of the interference pattern. Because

one of the mirrors is mounted to the stage, if the height of the stage is changing, so is the path difference. As a result the interference pattern is shifted. In the case where the path difference changes by $\Delta = \lambda/2$ the interference pattern changes from maximum in intensity to a minimum⁷. In an attempt to confirm that the travel of the stage is indeed $d = 350 \mu\text{m}$ per turn of the micrometer screw, the interference pattern is recorded with a photodiode. An aperture is used to remove everything but one of the stripes of the interference pattern. A trace of the photodiode signal is recorded while turning the micrometer screw. An excerpt of the result is shown in Figure 5.8. As the micrometer screw is turned the interference pattern shifts accordingly. Between two minima the height of the stage changes by $d = \lambda/2 \approx 316,5 \text{ nm}$ ⁸. By counting all minima the total change in height can be deduced.

While turning the micrometer screw by $\phi = 90(6)^\circ$ a total of $N = 234(10)$ minima are recorded. This results in a calculated displacement of $d_0 = 296(30) \mu\text{m}/\text{turn}$. The phase difference caused by a change in path difference is determined by $\varphi_0 = \cos(\alpha) \cos(\beta) d_1 - d_2$. The change of the angles has to be accounted for. Taking the worst-case change determined in the previous section the change in φ_0 as a result of the change in the angles is equivalent to $d_1 = 16(4) \mu\text{m}$. The displacement of the z -stage is thus given by

$$d = 300(50) \frac{\mu\text{m}}{\text{turn}}. \quad (5.3)$$

This is just within the expected value. However it should be noted that this method of measuring the travel of the stage is not ideal and can be improved by turning the micrometer screw multiple turns rather than a quarter turn.

During the travel-range measurements it was discovered that there is creeping right after adjusting the height. This creeping happens on a timescale of $t \sim 10 \text{ s}$ and is on the order of $d_{\text{creep}} = 2 \mu\text{m}$. This result is reproducible and is suspected to be caused by the z -stage settling down. Residual mechanical stress in the system right after adjusting the height may be a likely cause for this phenomenon.

Long-Term Stability

Long-term drifts of the stage have to be kept as small as possible. This is especially the case when experiments are performed over night without any supervision. If the long-term drift are too big as a measurement progresses the drift could lead to a defocusing of the

⁷ Note that because the light gets retroreflected at the mirror, the change in path difference is twice that of the displacement of the mirror.

⁸ In the experiment a HeNe-Laser with a wavelength of $\lambda \approx 633 \text{ nm}$ is used.

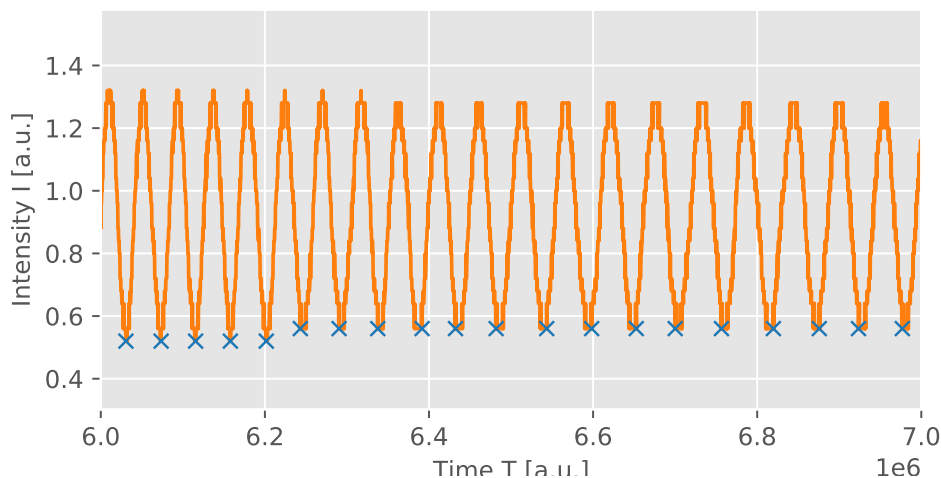


Figure 5.8.: A sequence of the of the signal recorded on the photodiode while adjusting the height of the z -stage. The photo diode is used to detect the interference pattern of the Michelson interferometer. An aperture is used in order to block all but the center stripe of the interference pattern. As the height of the z -stage is changed, a global phase shift changes the interference pattern. If the height is changed by $\Delta = \lambda/2$ the interference pattern shifts by $\Delta\phi = 2\pi$. For the experiment a laser with a wavelength of $\lambda = 633$ nm is used. Thus, the difference in height between two minima is $d \approx 316,5$ nm. By counting all the minima the total change in height can be calculated.

images, making them unusable.

In order to determine the long-term drift of the stage, the phase of the interference pattern has to be recorded. This is done by taking images of the interference pattern in regular intervals and calculating the phase for every image taken. Before the measurement is started, the Michelson interferometer is adjusted such that the striped pattern is vertical. This is done to simplify the image analysis. The phase of the interference pattern is determined by calculating the Fourier transform of the image. In the Fourier transform there is only one prominent peak, corresponding to the periodicity of the interference pattern. Thus, the phase of the interference pattern can be tracked. After the Fourier transform the phase lies in an interval between $(-\pi, \pi]$ and the resulting phase data is shown in Figure 5.9 a). Because the drifts are larger than this interval, jumps in the phase occur. These jumps of 2π have to be accounted for in order to track the phase over long times. The unwrapped data is shown in Figure 5.9 b). The data is taken shortly after the height of the stage is adjusted. In the first ≈ 30 min the phase changes by $\Delta\phi \approx -6\pi$, corresponding to a change in height of $\approx 1 \mu\text{m}$. After that, the phase stabilizes and fluctuations are now on the order of the expected change caused by thermal fluctuations. Assuming a thermal expansion coefficient of brass of $20 \cdot 10^{-6}/\text{K}$ and a total height of

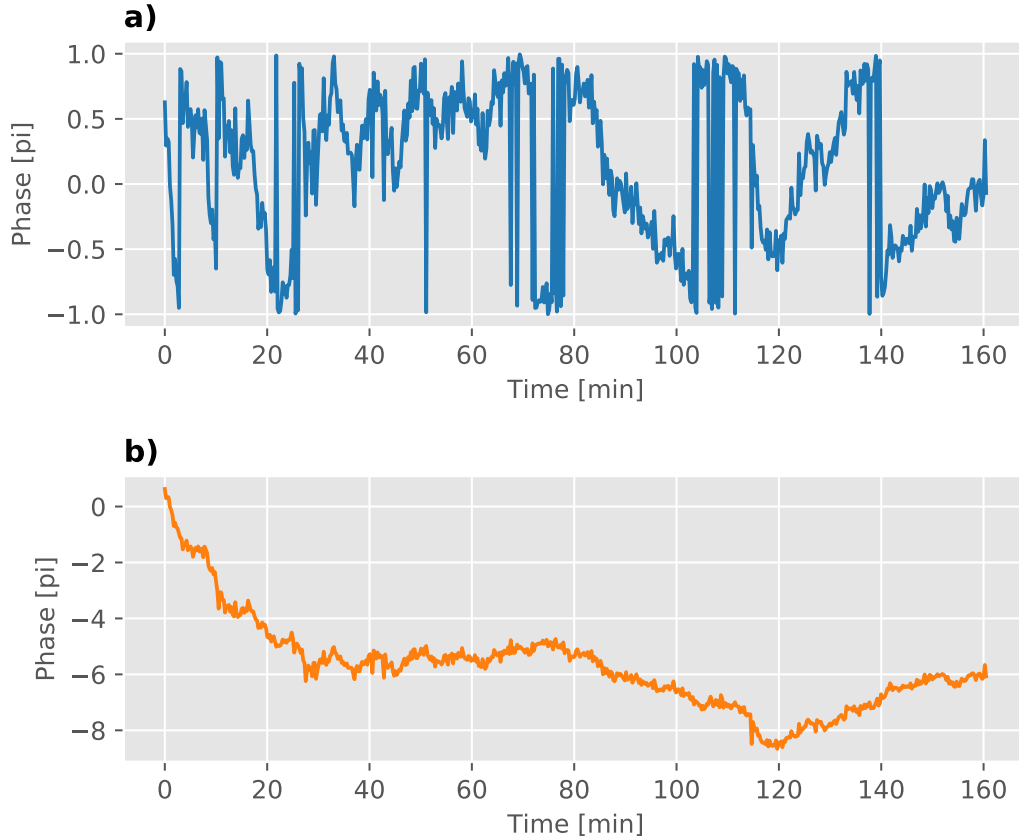


Figure 5.9.: Measurement of the long-term stability of the z -stage. Data is acquired by taking images of the interference pattern in regular intervals. The images are Fourier transformed. In the Fourier transform there is one prominent peak, corresponding to the periodicity of the interference pattern. The phase of the frequency corresponding to this peak is tracked over time. The resulting data is shown in a). The Fourier transform outputs the phase in an interval between $(-\pi, \pi]$. Because the drift is larger than this interval, the data has to be adjusted for 2π jumps. The unwrapped data is shown in b). Initially there is a change in the phase of $\Delta\phi \approx -6\pi$. Afterwards the data fluctuates on the order of $\Delta\phi \approx 1\pi$. These fluctuations are on the order of fluctuations caused by thermal fluctuations which are on the order of $\Delta\phi \approx 1.6\pi/K$.

the stage of ~ 10 cm, the change in phase due to thermal expansion is expected to be on the order of $\approx 1.6\pi/K$. Since the phase is moving both towards larger and smaller values, sagging of the stage over time is ruled out.

Summary

The z -stage is used for coarse positioning of the main-chamber objective. The travel range of the stage is 10 mm. The height can be adjusted by a micrometer screw with a pitch of $p = 350 \mu\text{m}$. Using a Michelson interferometer it was measured that the stage moves by

$d = 300(50) \mu\text{m}/\text{turn}$. If the height of the stage is changed, the tip-/ tilt can change by as much as $\Delta\alpha = 1.0(5) \text{ mrad}$. However, this can be reduced by pushing against the springs which are used to stabilize the stage, i.e. if the stage has to be adjusted by $\Delta h = -0.5 \text{ mm}$ going down 1 mm and then up again by 0.5 mm minimizes the change in the angles. There is a period right after adjusting the height where the stage is creeping that can be on the order of $d_{\text{creep}} = 2 \mu\text{m}$. The stage was also tested with respect to its long-term stability. It was determined that after the initial creeping of the stage, changes of the height are on the order of the ones caused by thermal fluctuations $\Delta h \approx 300 \mu\text{m}/\text{K}$.

5.3. Transversal Cooling

In order to achieve a large atom flux at the main chamber, the atoms are cooled transversely before entering the Zeeman slower. This is necessary because the Zeeman slower can only slow the atomic beam in the longitudinal velocity. Atoms that still have a non negligible transversal velocity can slowly drift towards the side wall of the vacuum chamber where they are lost. The cooling is done using the two-dimensional optical molasses technique described in Chapter 2.4.1. The interaction time between the atomic beam and the cooling laser, and thus the efficiency of the cooling, depends on size of the laser beam. In order to maximize the interaction time, the laser beam is widened along the propagation axis of the atomic beam (\boldsymbol{x} -axis). This is done with a cylindrical telescope. The setup is shown in Figure 5.10. At the atomic beam location the laser beam has a waist of $w_x = 30 \text{ mm}$ and $w_y = 3 \text{ mm}$. The beam is retroreflected after passing the atomic beam. As a result, two counter-propagating cooling beams interact with the atomic beam resulting in a one-dimensional optical molasses. An exact copy of the setup is installed such that the laser beams are orthogonal to the initial setup. This allows for efficient transversal cooling of the atomic beam in both directions resulting in a two-dimensional optical molasses.

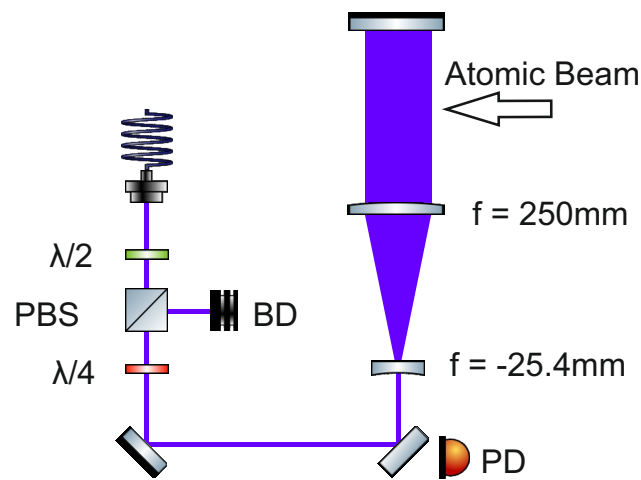


Figure 5.10.: Schematic of the setup used for the transversal cooling section. The light is collimated ($w_x = w_y = 3$ mm) using a fiber collimator. A half-wave plate and a polarizing beam splitter (PBS) are used to adjust the intensity of the cooling light and clean up the polarization. A quarter-wave plate is used in order to change the polarization of the retroreflected light such that it can be dumped in a beam dump (BD). The photodiode (PD) is used to monitor the cooling light intensity using the transmission of a backside-polished mirror. A cylindrical-lens telescope reshaped the beam such that the waists are $w_x = 30$ mm and $w_y = 3$ mm. The direction of the atomic beam is indicated by the arrow.

Atomic-Beam Spectroscopy

All experiments that are going to take place in the experimental apparatus start with a hot atomic beam of dysprosium. The atomic beam is first cooled transversely and subsequently slowed longitudinally. Atoms which are slowed down to $v \lesssim 8$ m/s can be trapped in a magneto-optical trap (MOT). The maximum number of atoms that can be trapped in the MOT depends on the flux of slow atoms at the main chamber. In order to optimize this flux the initial atomic beam has to be characterized both in terms of its spatial profile as well as in terms of its velocity distribution. In this chapter, the characterization of the atomic beam is described. The spatial profile of the atomic beam is measured and the influence of different temperature settings of the effusion cell is determined.

6.1. Effusion Cell

The hot atomic beam is created using an effusion cell¹. In the effusion cell, solid dysprosium is heated to temperatures below the melting point. At these temperatures some of the atoms leave the solid phase and enter a gaseous phase. These thermal atoms emerge from the oven and form an atomic beam. The beam is clipped by physical apertures in order to produce a nearly collimated atomic beam. A schematic of the setup is shown in Figure 6.1. The effusion cell is a dual-filament design. The solid dysprosium is loaded into the effusion cell (EC) part of the oven. A hot lip (HL) is placed in front of the EC. The HL is typically operated at temperatures slightly higher than the EC to prevent the apertures from clogging up over time as dysprosium is deposited on the apertures. Both the EC and HL are surrounded by a water-cooled enclosure. Additionally a multi-layer heat shield is placed $l = 17.5$ mm away from the aperture of the HL. The flux of the atomic beam emerging from the oven depends on the vapour pressure. This vapour pressure can be calculated using the Antoine equation

$$\log(p) = A - \left(\frac{B}{(C + T)} \right), \quad (6.1)$$

¹ CreaTec Fischer & Co. GmbH - Dual Filament Effusion Cell

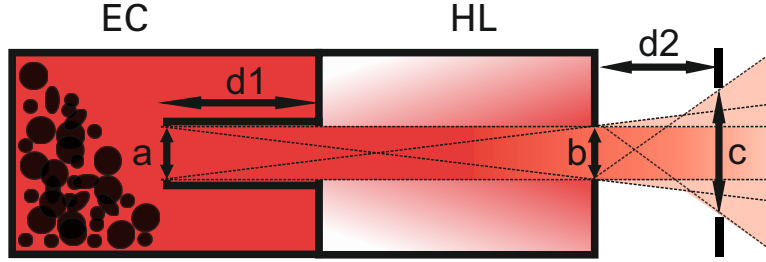


Figure 6.1.: Schematic setup of the effusion cell used in the experiment. The effusion cell is a dual filament design. It includes two separate sections that are individually heated. The effusion cell (EC) and the hot lip (HL). The two sections are separated by a $d1 = 20$ mm long tube with a diameter of $a = 3$ mm. The solid dysprosium is loaded in to the EC where it is typically heated to $T_{EC} = 1100^\circ\text{C}$. The HL is typically heated to a temperature of $T_{HL} = 1150^\circ\text{C}$. This is done in order to prevent the aperture from clogging up over time. The hot atomic beam can leave the HL through an aperture with a diameter of $b = 3$ mm. A multi-layer heat shield is placed $l = 17.5$ mm away from the aperture of the HL. The heat shield also acts as a third aperture with a diameter of $d2 = 17$ mm. The dashed lines indicate the atomic beam emerging from the EC and HL. The figure is not to scale.

where p is the pressure, T is the temperature and A , B and C are empirical constants that are different for each element. In the case of dysprosium the constants used are $A = 7.27(1)$, $B = 11192.30(1)$ and $C = 102.63(1)$. The constants are acquired by fitting the Antoine equation to the available data for the vapor pressure of dysprosium at various temperatures provided in [Lid04]. The resulting vapour pressure as a function of temperature is shown in Figure 6.2. As the temperature increases the vapour pressure increases exponentially. At temperatures $T < 600^\circ\text{C}$ virtually no dysprosium can be detected exiting the oven.

The thermal atoms emerging from the heated up dysprosium can be considered as an ideal gas stored in a box. In thermal equilibrium this ideal gas is described by the ideal gas law

$$p = k_B n T, \quad (6.2)$$

where p is the pressure, k_B is the Boltzmann constant, n is the atomic density and T is the temperature. Because the effusion cell is placed inside a vacuum chamber², the pressure gradient between the EC and the vacuum causes the atoms to escape. During this process, atoms can collide with each other and with the walls of the chamber. The atom-atom

² The pressure in the vacuum chamber is $p \sim 10^{-10}$ mbar.

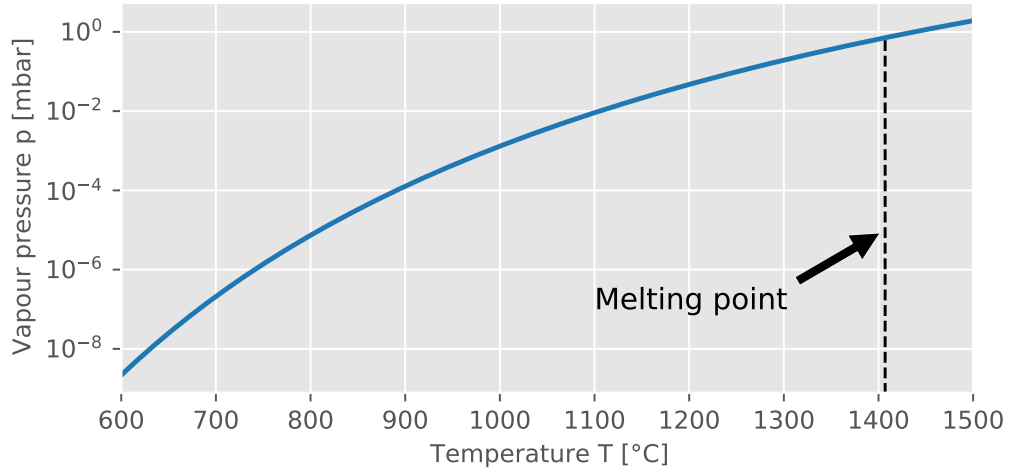


Figure 6.2.: Vapour pressure of dysprosium as a function of temperature that is calculated using the Antoine equation (Eq. (6.1)). Typical operating temperatures for the effusion cell in the experiment are between $T = 1100\text{ °C}$ and $T = 1200\text{ °C}$. At these temperatures the atom flux is large enough for efficient loading of the MOT and subsequent experiments. As a reference, the melting point of dysprosium is indicated by the dashed line.

collisions are characterized by the mean free path Λ which is given by [Dem18]

$$\Lambda = \frac{1}{n\pi d^2}, \quad (6.3)$$

where d is the diameter of the atomic species. There are two distinct regimes depending on the density of the gas. If Λ is smaller than the size of the aperture, the atoms collide while emerging from the EC. This regime is called the hydrodynamic flow regime. This is a regime where the collective transport is described based on fluid dynamics. In the second regime, if Λ is larger than the aperture, atom-atom collisions are rare and the atom-wall collisions dominate. This regime is called the effusive regime giving the name to the effusion cell as this is the regime where the effusion cell is said to operate. In this effusive regime the velocity distribution of the atomic beam emerging from the EC can be described by the Boltzmann distribution introduced in Eq. (2.31).

6.2. Atomic-Beam Characterization

In order to characterize the atomic beam, the spatial profile as well as the velocity distribution has to be determined. This is done by making use of the spectroscopic techniques described in Chapter 2.3. A probe beam with a wavelength of $\lambda = 421\text{ nm}$ is

set up orthogonal to the atomic beam and adjusted such that the probe beam is incident with the center of the atomic beam. After the probe beam has passed the atomic beam it is detected using an amplified photodiode. Additionally a reference photodiode is used to monitor the power of the probe beam. A CMOS camera with a two-lens objective is used to image the fluorescence of the atomic beam. Optical bandpass filters centered around 420 nm are used in front of the photodiodes as well as the camera in order to filter out the background signal. The schematic of the setup is shown in Figure 6.3.

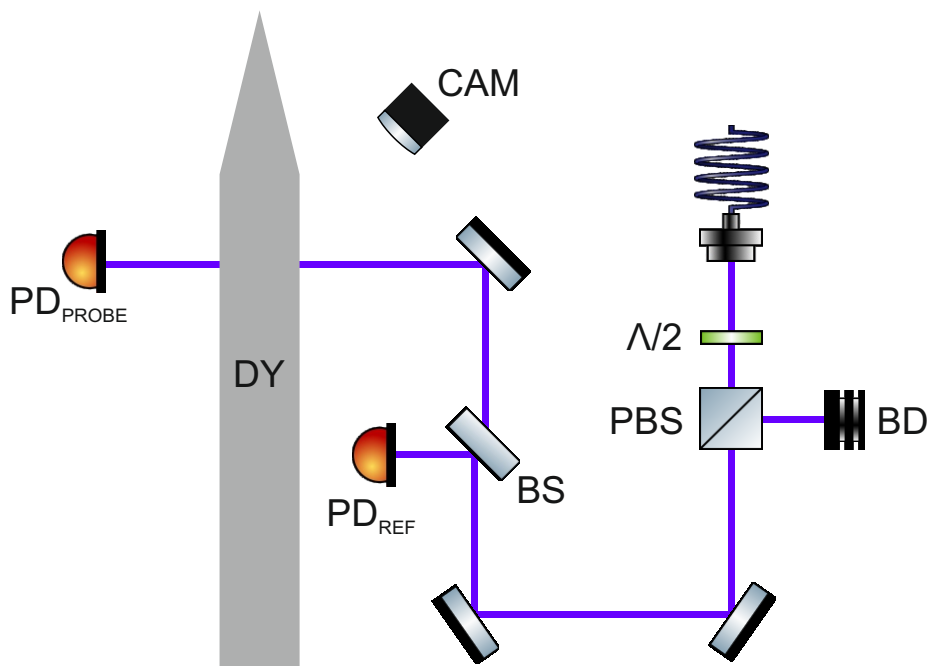


Figure 6.3.: Schematic of the setup used for the atomic beam characterization using the 421 nm transition of dysprosium. The intensity of the probe beam can be adjusted using a half-wave plate ($\lambda/2$) and a polarizing beam-splitter cube (PBS). A 50:50 non polarizing beam-splitter (BS) is used to separate the probe beam into two beams with equal power. One of these beams is detected on the reference photodiode (PD_{ref}), the other beam is detected on the probe photodiode (PD_{probe}) after the probe beam has passed through the atomic beam of dysprosium (DY). A camera (CAM) is used to measure the fluorescence signal. The probe beam is orthogonal to the atomic beam and aligned such that it is incident with its center. The probe- and reference photodiodes are used for measuring the absorption spectrum. The camera is mounted orthogonal to both the atomic beam and the probe beam. This allows the camera to image the spatial profile of the atomic beam. The photodiodes and camera are fitted with optical bandpass filters centered around 420 nm in order to filter out the background.

6.2.1. Transversal-Velocity Distribution

In a first step, the atomic beam is characterized using absorption spectroscopy. As the frequency of the probe beam is scanned, the voltage of both the reference photodiode (PD_{ref}) and the probe photodiode (PD_{probe}) are recorded. The two individual traces are shown in Figure 6.4 a). The absorption signal is calculated by dividing the two photodiode voltages. This allows for the measurement to be independent of power fluctuations that occur during the frequency scan. The resulting absorption profile is shown in Figure 6.4 b). There are two main peaks in the absorption signal. The peak at lower frequencies corresponds to ^{164}Dy , while the one at higher frequencies is assigned to ^{162}Dy . There are also several smaller peaks. These peaks correspond to transitions involving other bosonic isotopes and the hyperfine structure of the fermionic isotopes. The absorption spectrum is limited by the Doppler shift. While this limits the visibility of the individual peak. The Doppler profile can be used in order to estimate the transversal velocity of the atomic beam. This is done by fitting a Gaussian profile to one of the absorption peaks. As was discussed in Chapter 2.2.2, the width of this Gaussian profile can be used in order to calculate the velocity. In the example shown in Figure 6.4, the width of the Doppler broadened profile is $f_{\text{FWHM}} = 300(40)$ MHz resulting in a transversal velocity of $v_{\text{trans}} = 50(10)$ m/s. Note that this derivation assumes that the velocity distribution of the beam is in agreement with the Boltzmann distribution (Eq. (2.31)) However, the velocity distribution is modified and does not follow the Boltzmann distribution.

6.2.2. Spatial Beam Profile

The spatial beam profile of the atomic beam is measured by imaging the fluorescence of the atomic beam with a CMOS camera³ orthogonal to the probe beam. The probe beam is tuned close to the resonance of the 421 nm transition of dysprosium. As was discussed in the previous section, due to its high temperature, the atomic beam exiting the effusion cell has a transversal velocity of $v_{\text{trans}} \sim 50$ m/s. Because the Doppler shift for these velocities is larger than the linewidth of the probe laser, the frequency of the probe beam has to be scanned in order to image the whole atomic beam profile. Some sample images of such a scan of the probe frequency are shown in Figure 6.5 a)-c). Between two images the frequency is shifted by $\Delta f \approx 60$ MHz⁴. In Figure 6.5 a) the probe frequency is red detuned with respect to the resonance of the atomic transition⁵. As the probe

³ FLIR Blackfly S, BFS-U3-63S4M

⁴ The repetition rate is limited mainly by the exposure time of the camera.

⁵ If the laser frequency is red detuned, $\omega_{\text{laser}} - \omega_0 < 0$.

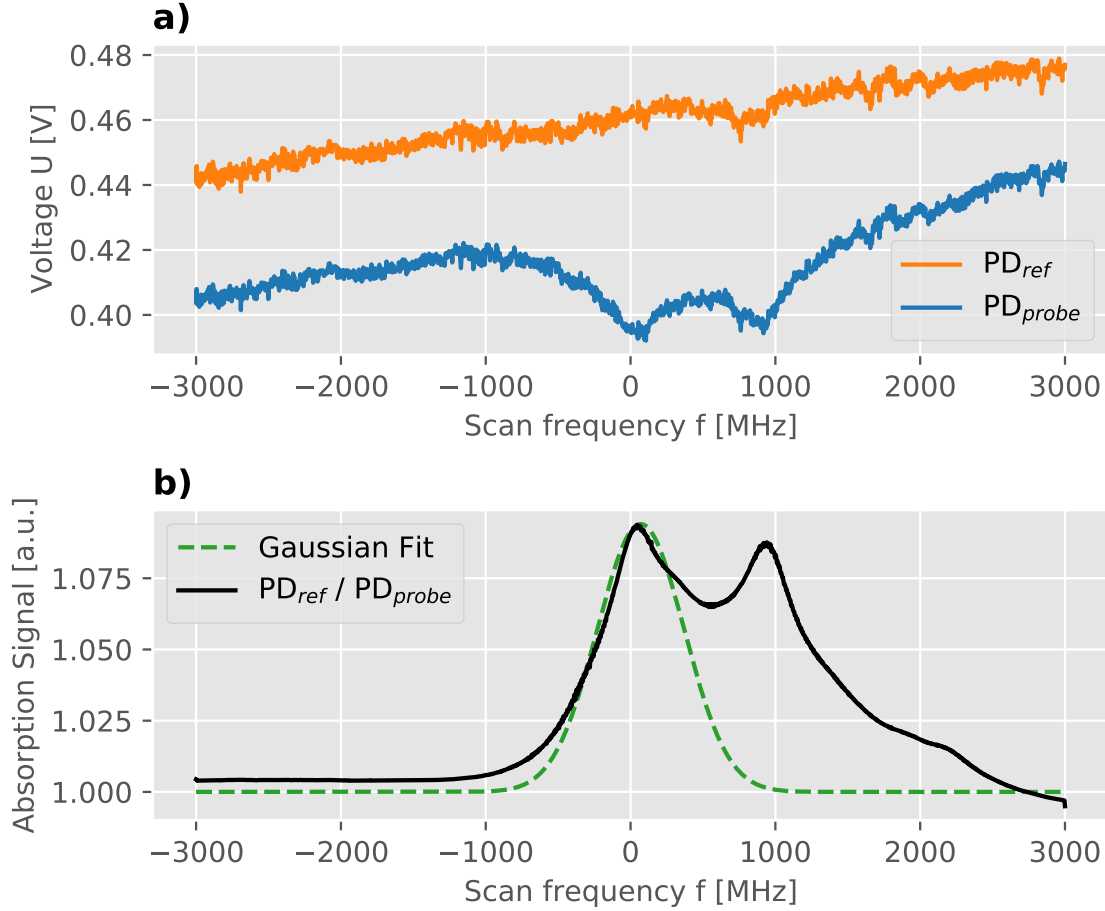


Figure 6.4.: Absorption spectroscopy of the atomic beam using the 421 nm transition of dysprosium. The probe beam is positioned orthogonal to the atomic beam and adjusted such that it intersects the center of the atomic beam. In a) the two individual signals of the probe and reference photodiode are shown. The probe photodiode detects the probe beam after it has passed the atomic beam. The reference photodiode is installed before the atomic beam and is used to monitor the power during the scan. The absorption signal is obtained by dividing the signal of the reference photodiode by the probe. This is done in order to be unaffected by the power fluctuations that might occur during the scan. The resulting signal is shown in b). There are two distinct peaks which are assigned to the two bosonic isotopes ^{164}Dy and ^{162}Dy respectively. Several other, weaker peaks are visible around $f = 200$ MHz, $f = 1500$ MHz and $f = 2200$ MHz. These peaks correspond to transitions involving the other bosonic isotope (^{160}Dy) and the hyperfine structure of the fermionic isotopes ^{163}Dy and ^{161}Dy . The peak corresponding to ^{164}Dy is fitted with a Gaussian profile. The FWHM of the Gaussian profile is $f_{\text{FWHM}} = 300(40)$ MHz.

beam is tuned closer to the atomic resonance, the peak of the fluorescence moves towards the center of the atomic beam. This can be explained by the large transversal velocity of the atomic beam. Atoms move away from the center according to their transversal

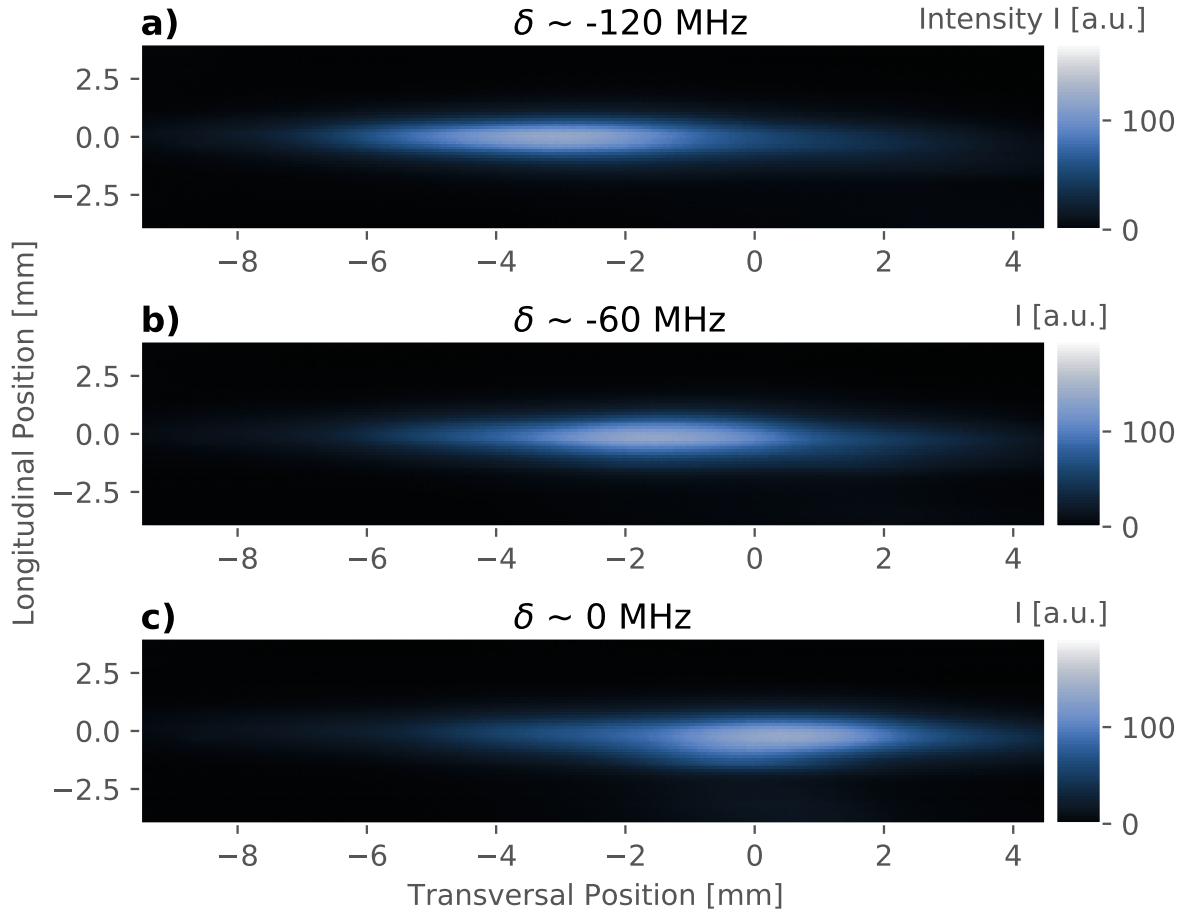


Figure 6.5.: Fluorescence images of the atomic beam, recorded during the frequency scan of the probe beam. The frequency spacing between two images is $\Delta f \approx 60 \text{ MHz}$. In a) the probe frequency is red detuned with respect to the resonance of the atomic transition. As the probe beam is tuned closer to the atomic resonance, the peak of the fluorescence moves towards the center of the atomic beam. This is shown in figures b) and c). This can be explained by the Doppler shift. In the rest frame of atoms moving against the probe beam, the frequency of the probe is shifted towards the blue. As a result they are resonant with the red detuned probe light (figure a). Atoms closer to the center of the atomic beam have smaller transversal velocities and are thus resonant with the probe beam if it is less red detuned.

velocity. As a result, the atomic beam diverges. Atoms which are far away from the center have the largest transversal velocity and experience the largest Doppler shift. In order to be resonant with the atoms the probe beam has to be detuned accordingly. In the center of the atomic beam, the atoms have negligible transversal velocities and as a result, experience no Doppler shift.

The whole scan is shown in Figure 6.6. Here, the individual images are integrated along the longitudinal axis in order to obtain the 1-dimensional fluorescence signal. During

the scan, multiple peaks in the fluorescence signal are detected. The strength of each peak depends on the abundance of the corresponding isotope and in the case of fermionic isotopes the strength of the individual hyperfine transitions. The two strongest peaks are assigned to the two bosonic isotopes of dysprosium with the largest natural abundance, namely ^{164}Dy and ^{162}Dy . The peak of a third bosonic isotopes, ^{160}Dy , although weak, can also be detected. The other peaks are assigned to transitions of the two fermionic isotopes, ^{163}Dy and ^{161}Dy . The assignment of the peaks is done using the data for the individual shifts provided in [LCB09].

As the laser frequency is scanned, different velocity classes of the atoms are resonant with the probe beam. In order to measure the full spatial profile of the atomic beam, the exposure time of the camera is set to times much longer than the duration of the frequency scan of the probe beam. As a result all velocity classes of the atoms are resonant with the probe beam at some point during the time the image is exposed. Thus, the whole atomic beam can be imaged. One such measurement of the atomic beam profile is shown in Figure 6.7 a). The effusion cell is operated at $T_{\text{EC}} = 1100^\circ\text{C}$ and $T_{\text{HL}} = 1150^\circ\text{C}$. The probe laser frequency is scanned from far red detuned to far blue detuned within $T_{\text{scan}} = 2\text{ s}$ and the exposure time of the camera is set to $T_{\text{camera}} = 20\text{ s}$. The probe power is set to $P_{\text{probe}} = 60\ \mu\text{W}$ to avoid overexposure the recorded image. In Figure 6.7 b) the fluorescence image is integrated along the longitudinal direction in a small box around the center of the probe beam to obtain a 1-dimensional atomic beam profile. On the edges, the spatial profile of the atomic beam has a slight asymmetry. The 421 nm transition of dysprosium is rather strong with a saturation intensity of $I_{\text{sat}} = 56.4\text{ mW/cm}^2$. As was discussed in Chapter 2.1.2, as the probe beam passes through the atomic beam the intensity decreases exponentially. Because the detected fluorescence depends on the intensity of the probe beam this effect is able to distort the atomic beam profile, especially at low probe power. As the asymmetry persists even for large probe powers $P > 1\text{ mW}$ and the low probe power is ruled out as the cause of the asymmetry.

6.2.3. Effusion-Cell Dynamics

If the effusion cell is working as expected, the atoms should emerge from the EC. Under the assumption that the effusion cell is operating in the effusive regime the trajectory of the atoms emerging from the EC or HL can be modeled as collision-free until they hit a wall where they are deposited. The atoms can be re-emitted if the temperature of the wall is high enough. Because of the geometry of the system, atoms that are emitted from the EC have a more narrow spatial profile as the ones emitted from the HL. This is

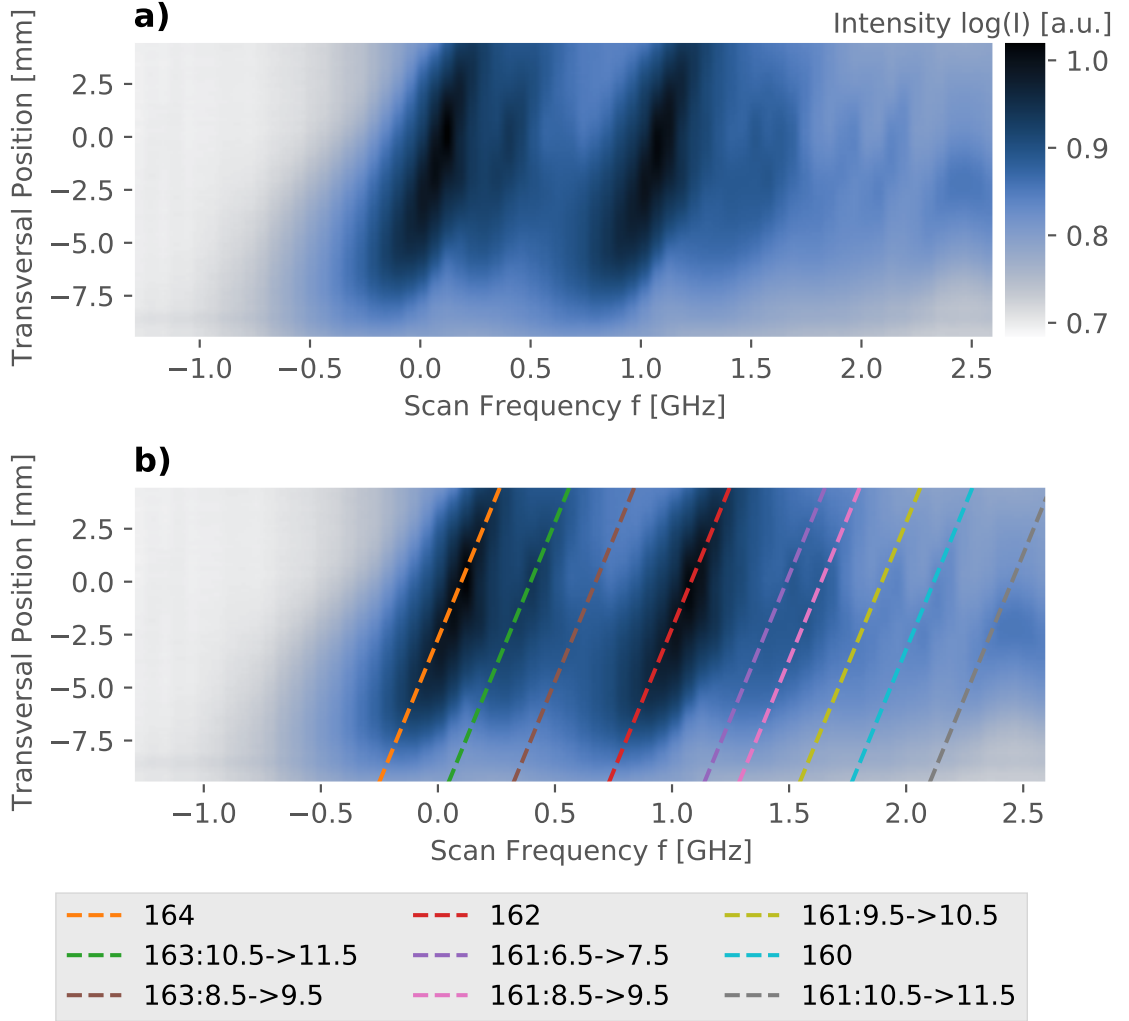


Figure 6.6.: Fluorescence images of the atomic beam during a frequency scan of the probe beam. The individual images are integrated along the longitudinal direction of the atomic beam. The frequency shift between two images is $\Delta f \approx 60$ MHz. The individual traces correspond to the different isotopes and hyperfine transitions of dysprosium. Because of the Doppler shift, traces move along a diagonal as the probe beam is scanned. Atoms that are on the edge of the atomic beam have large transversal velocities and therefore experience the largest shift. In the case where the movement of the atoms opposes the probe beam, this shift is towards the blue (i.e. higher frequencies). As a result, these fast atoms are resonant with a red detuned probe beam. In b) the individual traces are assigned to their corresponding transitions. The transitions are identified using the data provided in [LCB09]. For the measurement the effusion cell is set to $T_{\text{EC}} = 1100^\circ \text{C}$ and $T_{\text{HL}} = 1150^\circ \text{C}$.

also indicated by the dashed lines in Figure 6.1. Based on purely ballistic calculations, if the atomic beam is emitted from the EC, the diameter of the atomic beam should be $d \approx 4.5$ mm at the position where it is imaged. If the atoms are emitted from the HL, the

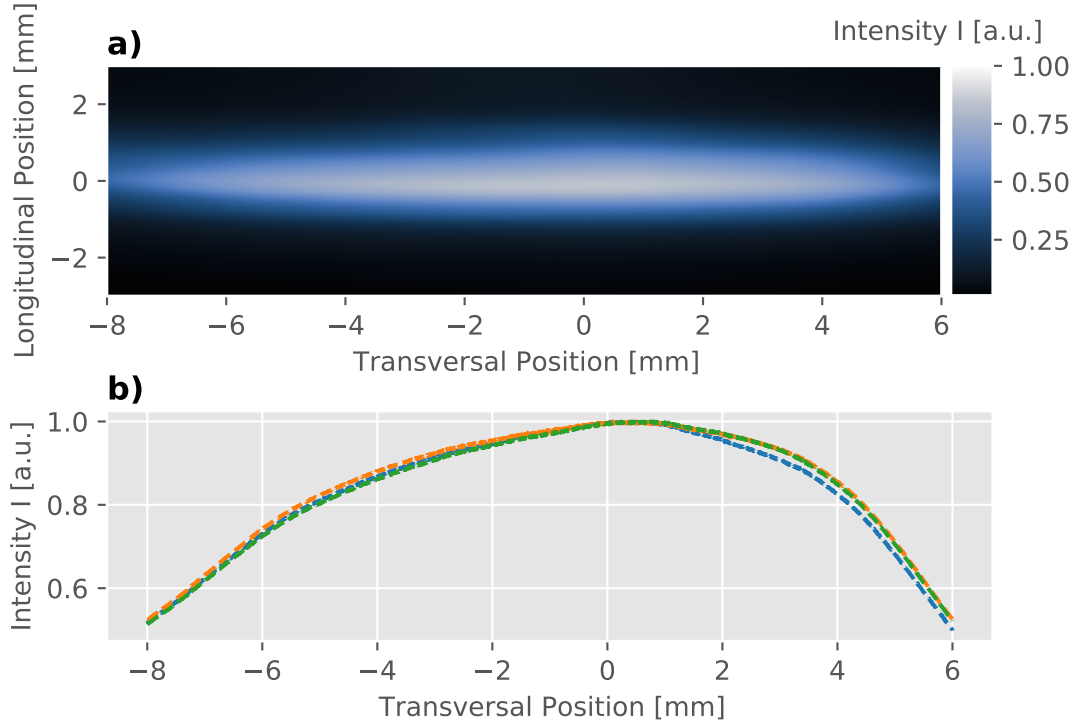


Figure 6.7.: Fluorescence image of the atomic beam profile. The image is recorded by setting the exposure time of the camera is set to $T_{\text{camera}} = 20$ s and simultaneously scan the probe frequency with a period of $T_{\text{scan}} = 2$ s. The resulting image is shown in a). In order to obtain the spatial profile of the atomic beam, a box around the center of the atomic beam is integrated along the longitudinal direction. The measurement is repeated multiple times and the result is shown in b). The atomic beam profile has a slight asymmetry at the edges. The profile is quite broad with a small peak around the center. Between the different measurements there are slight differences which could be an artifact of the trigger of the camera not being synced up with the scan. Note that the image does not capture the whole atomic beam because the field of view is not large enough. In this measurement the effusion cell is set to $T_{\text{EC}} = 1100^\circ\text{C}$ and $T_{\text{HL}} = 1150^\circ\text{C}$.

atomic beam diameter should be $d \approx 30$ mm, which is bigger than the field of view of the camera.

In order to test whether the atomic beam emerges from the EC or the HL, the atomic beam profile is measured for different temperatures of the EC and HL of the effusion cell. Because the vapour pressure and thus the atomic flux depends on the temperature, if one section, either EC or HL, is much hotter than the other one the majority of the atoms originates from the hotter section. Because of limitations of the effusion cell, the temperature difference between the two sections cannot be set to arbitrary large values as there is cross-talk between them. It is possible to heat the HL to temperatures higher than the EC by up to $T_{\text{HL}} - T_{\text{EC}} = 300^\circ\text{C}$, but it is not possible to do the opposite. The maximum

temperature difference between a hot EC and colder HL achieved is $T_{\text{EC}} - T_{\text{HL}} = 60^\circ\text{C}$. As a result, while the EC can be effectively turned off, that is not the case for the HL. Still, a difference in the atomic beam profile is observed. The atomic beam profiles for different temperatures for T_{HL} and T_{EC} are shown in Figure 6.8. As the temperature of the HL is lowered, the influence of the HL on the atomic beam profile decreases. Simultaneously, the influence of the EC is increased. Comparing the atomic beam profiles, there is a trend towards more narrow profiles as the influence of the HL is reduced. This is in line with the expectation due to the geometry of the system. However, the influence of the HL cannot be completely removed. At $T_{\text{EC}} = 1025^\circ\text{C}$ and $T_{\text{HL}} = 990^\circ\text{C}$ in addition to the narrow peak at the center, there is a broad background which is caused by the HL. As a result the atomic beam has a bimodal distribution. The amplitude of the two individual distributions can be adjusted by changing the temperatures of the EC and HL. Additionally, as the atomic beam narrows, the center of the atomic beam shifts to the left. This could be an indication that the EC and HL are slightly misaligned. It should be noted that, for the normal operating temperatures of $T_{\text{EC}} = 1100^\circ\text{C}$ and $T_{\text{HL}} = 1150^\circ\text{C}$, the atomic beam profile is closer to the broad profile indicating that atoms are primarily being emitted from the HL rather than the EC. Also, as the temperature of the HL is decreased the flux of the atomic beam is drastically reduced.

From the atomic beam profiles it can be assumed that the atomic beam is not emitted from the EC but rather directly from the HL. In order to confirm this assumption, the temperature of the EC is set to a temperature far lower than the operating temperature while HL is kept at $T_{\text{HL}} = 1150^\circ\text{C}$. In order to maximize the temperature difference the EC is set to $T_{\text{EC}} = 900^\circ\text{C}$. From previous measurements it is known that at temperatures $T \leq 900^\circ$ the vapour pressure of dysprosium is too low for a bright atomic beam and thus virtually no atoms are expected to be emitted from the EC. Therefore, a decrease in the absorption signal should be detected as T_{EC} decreases. During the measurement, the absorption signal is measured continuously as the temperature of the EC is changed. The result is shown in Figure 6.9. The measurement starts with $T_{\text{EC}} = 1100^\circ\text{C}$ and $T_{\text{HL}} = 1150^\circ\text{C}$ and during the measurement, the temperature of the effusion cell is decreased in three discrete steps. The temperature is actively decreased with a linear rate set by the internal controller of the effusion cell. After the new set-temperature is reached the system is allowed time to thermalize before the next step is initiated. First, the temperature of the EC is decreased to $T_{\text{EC}} = 900^\circ\text{C}$ while the HL temperature stays constant at $T_{\text{HL}} = 1150^\circ\text{C}$. The temperature is reached after ≈ 20 min and no significant change in the absorption signal is detected. The system is allowed to thermalize for

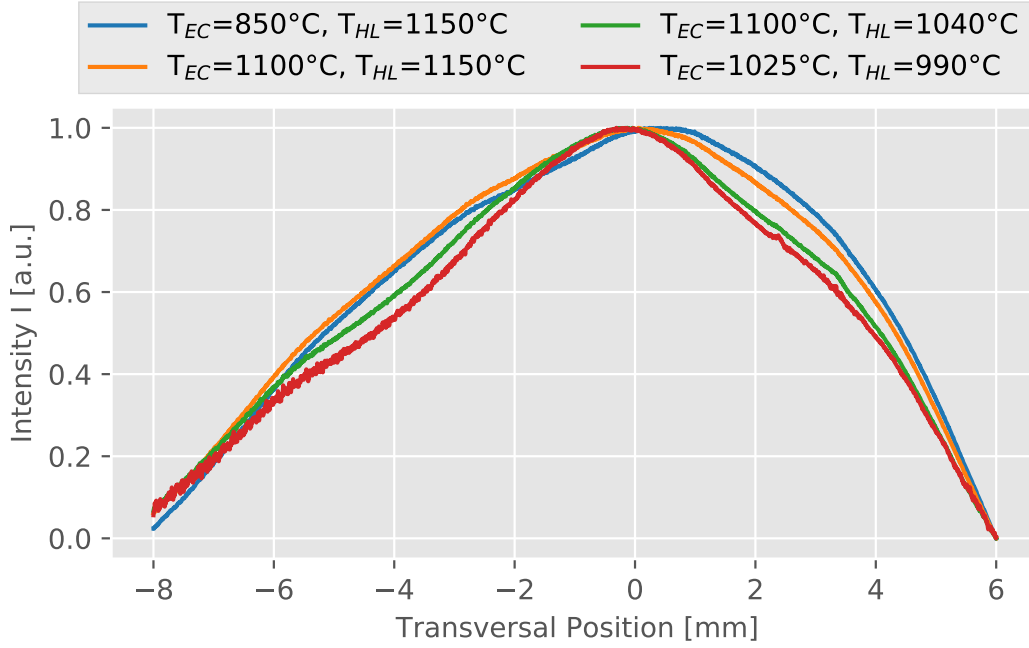


Figure 6.8.: Comparison of the atomic beam profile for different setting of T_{EC} and T_{HL} . The profiles are normalized in order to make it easier to compare them with each other. The atomic flux depends on the temperature, by changing the temperature of the EC and HL their influence on the atomic beam can effectively be tuned. Due to cross talk between the two regions, the temperature difference cannot be set to arbitrary values. For $T_{EC} = 850^\circ\text{C}$ and $T_{HL} = 1150^\circ\text{C}$ the majority of atoms is emitted by the HL. The resulting beam profile thus, mainly depends on the HL. In the experiment a broad distribution is observed which is inline with expectations. For $T_{EC} = 1025^\circ\text{C}$ and $T_{HL} = 990^\circ\text{C}$ the opposite is the case and the majority of atoms emerge from the EC. Here, a narrow peak on top of a broad distribution is observed. This is due to the fact that at $T_{HL} = 990^\circ\text{C}$, the HL still contributes to the atomic flux and thus also the beam profile. At the normal operating regime of $T_{EC} = 1100^\circ\text{C}$ and $T_{HL} = 1150^\circ\text{C}$, the atomic beam is dominated by the broad distribution caused by the HL. It should be noted that for measurements with a reduced HL temperature, the probe power had to be increased by a factor of 20, indicating that the atomic flux in this operating regime is drastically decreased.

≈ 40 min during which a very slight decrease in the absorption is measured. In a next step, the temperature of the EC is held constant at $T_{EC} = 900^\circ\text{C}$ and the temperature of the HL is decreased to $T_{HL} = 950^\circ\text{C}$. Immediately a decrease in absorption is detected. The absorption signal decreases further even after the new set point is reached. This is an indication that the system has not yet fully thermalized as it reaches the set-temperature. In a last step both the EC and HL temperatures are decreased to $T_{EC} = 600^\circ\text{C}$ and $T_{HL} = 650^\circ\text{C}$. The absorption decreases further and the measurement is stopped when the signal on-resonance and off-resonance can no longer be distinguished. At this point virtually no atoms are emitted from the effusion cell. The measurement is repeated and

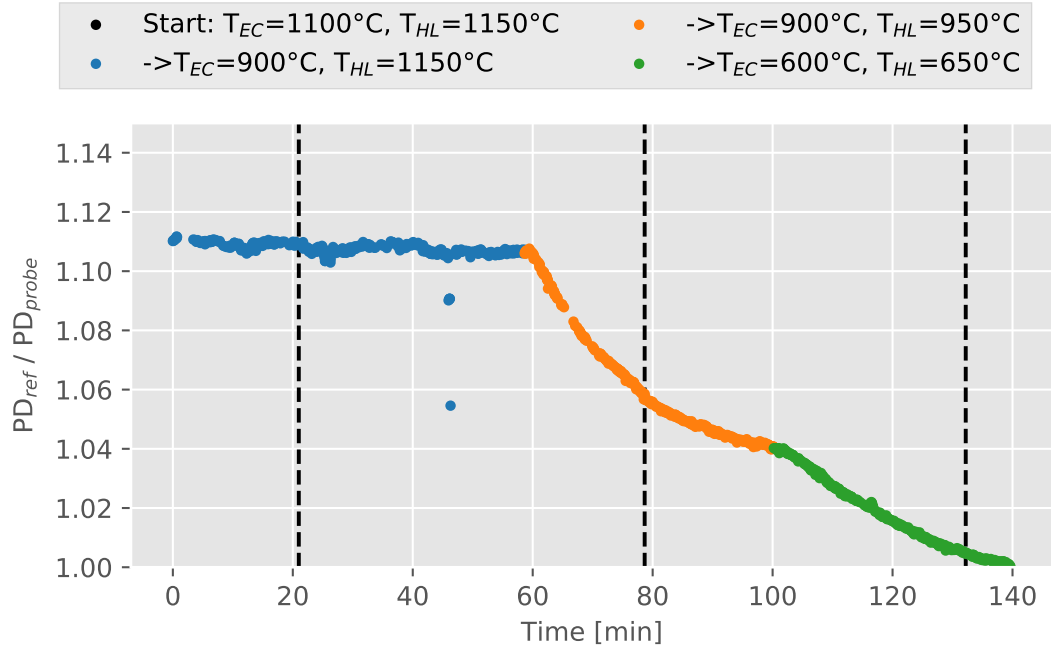


Figure 6.9.: Absorption signal during a cooling sequence of the effusion cell. During the measurement the probe laser is kept on resonance. Changes in the absorption signal are therefore a direct indication of a change in atom flux. The data is rescaled such that $PD_{ref}/PD_{probe} = 1$ for low temperatures or for a probe frequency far off resonance. The temperature is changed in three steps indicated by the different colours. The dashed lines indicate the time where the new set temperature is reached. The system is allowed to thermalize after the new set temperature is reached. The experiments starts with $T_{EC} = 1100^{\circ}\text{C}$ and $T_{HL} = 1150^{\circ}\text{C}$. In a first step the temperature of the EC is lowered to $T_{EC} = 900^{\circ}\text{C}$. Even after $T = 40$ min of thermalization there is no significant change in the absorption signal, indicating that the atom flux did not change between the two temperature settings. In a second step the temperature of the HL is lowered to $T_{HL} = 950^{\circ}\text{C}$. Immediately the absorption signal decreases. The signal decreases further after the new set temperature is reached. In a last step both the temperatures are lowered to $T_{EC} = 600^{\circ}\text{C}$ and $T_{HL} = 650^{\circ}\text{C}$. The measurement is stopped when the signal with a probe beam on resonance can no longer be differentiated from the signal with a probe beam far off resonance.

the same behaviour is observed.

From this measurement it can be concluded that the atoms do emerge from the HL. One explanation for this behaviour is that the EC is continuously loading the HL with dysprosium atoms. As the vapour pressure inside the HL increases, the HL starts to behave like the EC and the atomic beam is emitted by the HL.

6.2.4. Summary

The atomic beam is produced using a dual filament effusion cell. It consists of two regions, the effusion cell EC and hot lip HL. The temperature of the EC and HL can be adjusted separately. However, due to limitations of the effusion cell the temperature difference cannot be set to arbitrary values. The atomic beam exiting the effusion cell was characterized using spectroscopic techniques. First the atomic beam is characterized using absorption spectroscopy. By fitting a Gaussian distribution to one of the absorption peaks, the transversal velocity is determined to be $v_{\text{trans}} = 50(10)$ m/s. The spatial beam profile is measured using fluorescence imaging. The atomic beam has a broad distribution indicating that the atoms are emitted from the HL rather than the EC. This is confirmed by measuring the atom flux in the atomic beam for various temperatures of EC and HL. In the normal operating regime where $T_{\text{EC}} = 1100^\circ\text{C}$ and $T_{\text{HL}} = 1150^\circ\text{C}$, the majority of the atoms emerge from the HL. It is concluded that in the normal operating regime the HL has EC characteristics. For the experiment this means that, while the HL is able to prevent clogging of the apertures over time, it also results in the aperture of the EC not working as intended. As a result the atomic beam is much broader than expected. The effusion cell is not operating in a strictly effusive regime. Thus, hydrodynamics could play a role in the atomic beam characteristics.

Conclusion

This master thesis describes the design and characterization of several components of a novel quantum gas microscope for dysprosium atoms.

In the experimental apparatus, several magnetic-field coils are used in order to precisely control the magnetic field. Three large rectangular Helmholtz coil pairs are used to compensate external magnetic fields. The coils are designed to produce a homogeneous magnetic field in x-, y-, and z-direction, respectively. The magnetic field generated in the center of the main chamber is $B_{x/y/z} \approx 1 \text{ G/A}$. The compensation coils can also be used in order to create offset fields or compensate small gradients that might exist. One pair of circular Helmholtz coils is used in order to generate large homogeneous fields in z-direction. They are also referred to as Feshbach coils, as they are mainly used in order to tune atom-atom interactions via so called Feshbach resonances. These coils produce a field of $B_z \approx 1.5 \text{ G/A}$ and are designed to operate at currents $I > 50 \text{ A}$. A pair of circular coils in an anti-Helmholtz configuration is used in order to generate the quadrupole field needed for the operation of the magneto-optical trap. The magnetic-field gradient produced in the center is $\nabla B_z \approx 1.5 \text{ (G/cm)/A}$ and $\nabla B_{x/y} \approx 0.7 \text{ (G/cm)/A}$. In the scope of this thesis, all of these coils were designed, wound and their magnetic fields were simulated.

In the main chamber of the experimental apparatus a high-resolution imaging system with a resolution of $r \approx 0.5 \mu\text{m}$ is implemented. The objective is positioned using a stack of positioning stages. A custom manual positioning stage is used for the coarse alignment. In this work, the custom stage was characterized using interferometric techniques. The stage has a travel range of $d \pm 5 \text{ mm}$, with a resolution of $r < 20 \mu\text{m}$. The stability of the tip- and tilt-angles during height adjustment is $\Delta\alpha < 1.5 \text{ mrad}$ and the long-term stability of the stage is on the order of drifts caused by thermal fluctuations.

All experiments start with the production of a hot atomic beam of dysprosium. This is done using a dual filament effusion cell consisting of an effusion cell (EC) where solid dysprosium is heated to $T \approx 1100 \text{ }^\circ\text{C}$ and a hot lip (HL) that acts like a heated aperture in order to prevent clogging. In this thesis, the spatial profile of the atomic beam was characterized using spectroscopic techniques and the influence of different temperatures of the EC and HL were determined. By doing absorption spectroscopy on the 421 nm

transition of dysprosium, the transversal velocity of the atomic beam was determined to be $v_{\text{trans}} = 50(10)$ m/s. Using fluorescence imaging, the spatial beam profile of the atomic beam was measured. The measurements indicate that the atoms are emitted by the HL. As a result, the atomic beam is much broader than expected and transversal velocities are larger. This result is contrary to the assumed working principle of the effusion cell, where it is assumed that the atomic beam originates from the EC.

Outlook

At the time of writing this thesis, the experimental apparatus is moving closer towards the production of ultracold quantum gases in the main chamber. The current status of the apparatus is shown below. All coils needed for the magnetic-field control at the main chamber are installed. By performing spectroscopy in the main chamber, first signs of transversal cooling and longitudinal slowing of the atomic beam were observed. After dysprosium atoms are successfully trapped in the 5-beam MOT, the positioning stages for the high-resolution imaging system can be installed. In the near future the glass-cell containing the solid-immersion lens needed for the single-site resolved quantum gas microscope will be added to the system. Here, the atoms will be trapped in an optical lattice in order to study, among other things, the dipolar Fermi-Hubbard model.

Appendix

A. Winding the Magnetic-Field Coils

Due to tight tolerances, great care has been taken to ensure that coil assembly containing both the gradient- and Feshbach coils can fit inside the recessed viewports of the main chamber. The gradient- and Feshbach coils are wound around an aluminium cylinder. A stamp is used in order to control the height of the coil during winding. To allow for smooth transitioning between the different layers of the coil, the rectangular wire used for the Feshbach coils is bent using a custom tool. The process of bending and winding the coil is depicted in Figure A.1 and Figure A.2. To ensure that the finished coil assembly can fit inside the recessed viewports of the experiment a mock-up version of the vacuum chamber is used for testing. This is shown in Figure A.3. Both the gradient- and Feshbach coils are epoxied to the brass support structure using Electrolube TCOR75S. The whole assembly is inserted into the recessed viewport of the main chamber and secured using titanium screws. The assembly containing both the gradient- and Feshbach coils in its assembled form is depicted in Figure A.4.

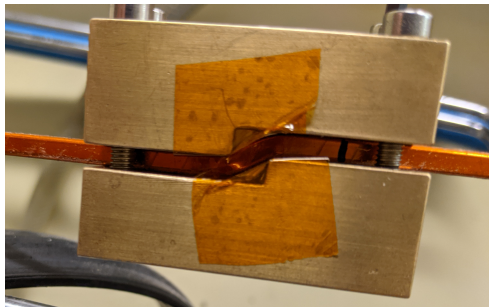


Figure A.1: Custom tool that is used in order to bend the rectangular, hollow copper wire. The straight wire positioned between two brass parts. The two brass parts can be carefully tightened using four screws. As they are tightened, the copper wire is bent. The result is a s-bend that displaces the copper wire by exactly the height of the wire.



Figure A.2: The coil is wound around an aluminium cylinder. A stamp is used to ensure that the height of the coil is up to specifications. Before the coil is wound around the cylinder the wire is pre-bend. In the image it is shown how these bends line up in order to allow the wire to transition to the next layer.

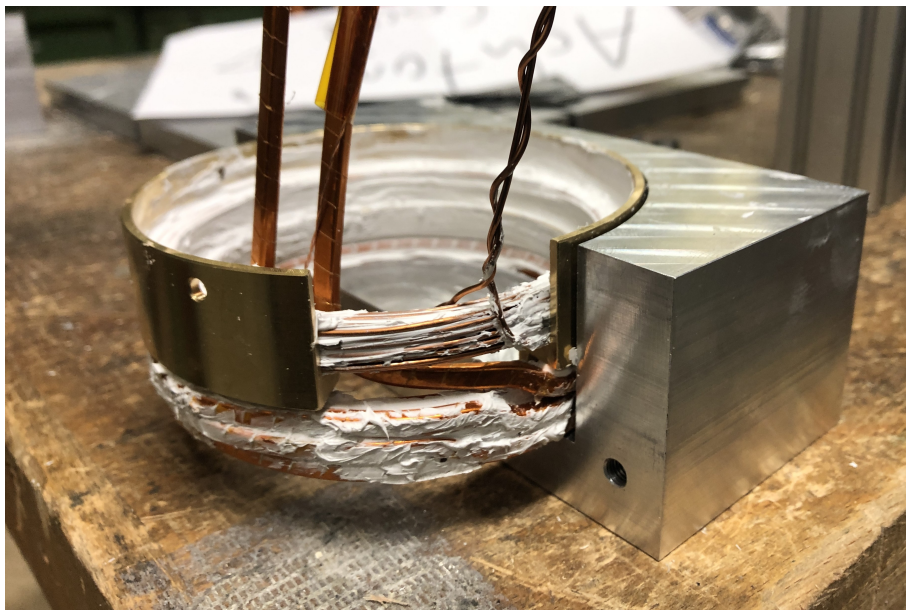


Figure A.3: The image shows the epoxied coil assembly in the mock-up version of the vacuum chamber. This mock-up is used to test whether the coil assembly can fit inside the recessed viewports. This mock-up is also used to hold everything together while the epoxy (Electrolube TCOR75S) dries. Image shows the epoxied coil assembly in the mock-up.

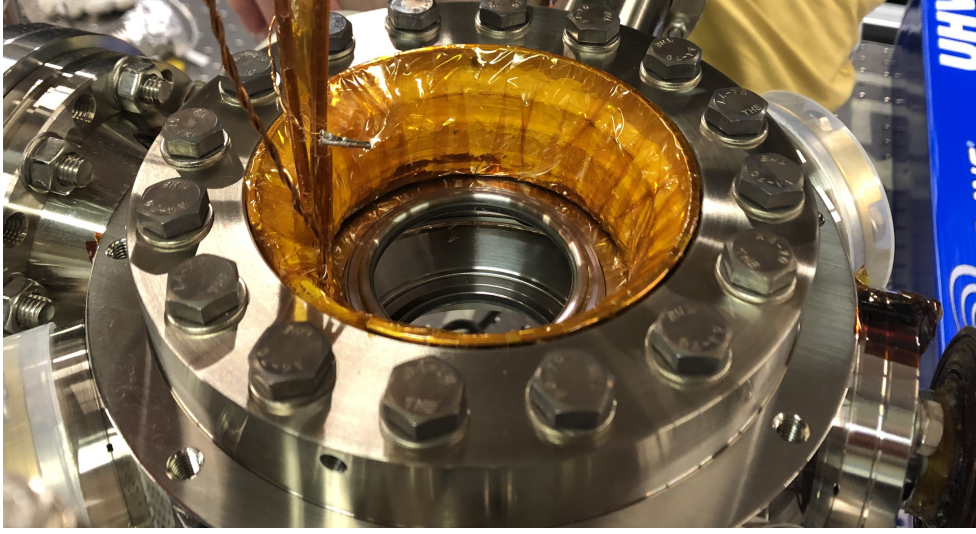


Figure A.4: Finished coil assembly in its final position in the recessed viewport. In order to protect against electrical shorts and in order to avoid small flakes of the epoxy to contaminate the viewport the assembly is wrapped in multiple layers of Kapton-tape.

B. Magentic-Field Simulation

The magnetic fields generated by the different coils are simulated using the Magpylib-package for Python. The Magpylib-package provides a fully vectorized implementation of solvers for permanent magnets as well as current distributions. The fields generated by currents are directly derived by solving the Biot-Savart law introduced in Chapter 3.1

$$\mathbf{B}(\mathbf{r}) = \frac{\mu_0}{4\pi} \int d^3\mathbf{r}' \nabla \times \left(\frac{\mathbf{j}(\mathbf{r}')}{|\mathbf{r} - \mathbf{r}'|} \right). \quad (\text{B1})$$

with the current distribution $\mathbf{j}(r)$ given by the individual coil geometry. The analytic expressions are also given in [Sim+01];[Mis00]. Circular coils, e.g. the Gradient- and Feshbach coils, are implemented as a circular current distribution. Rectangular coils, e.g. the compensation coils, are implemented as line currents that start and end at specific vertices. As an example the code that is used to calculate the field of the gradient coils is provided below.

```

1 # -*- coding: utf-8 -*-
2 """
3 Created on Mon Jul 26 17:41:50 2021
4
5 @author: Uerlings
6 """
7
8 import numpy as np
9 import matplotlib.pyplot as plt
10 import magpylib as magpy
11
12 # create a Magpylib collection of Circular Sources that form a coil
13 coil = magpy.Collection()
14 coil2 = magpy.Collection()
15
16 # geometry of our gradient/MOT-coils 6-6-6-6-6 winding pattern
17 # using 1mm diameter wire, all units in mm
18 R = 42.5
19 d = 37
20
21 #coil 1
22 for z in np.linspace(d,d+5,6):
23     for r in np.linspace(R,R+5,6):
24         winding = magpy.current.Circular(
25             current = 1,
26             diameter = 2*r,
27             position = (0,0,z))
28         coil += winding
29
30 #coil 2
31 for z in np.linspace(-d,-(d+5),6):
32     for r in np.linspace(R,R+5,6):
33         winding = magpy.current.Circular(
34             current = -1,
35             diameter = 2*r,
36             position = (0,0,z))
37         coil2 += winding
38
39 # create a grid
40 simlength=100
41 size=200
42 pos = np.linspace(-simlength,simlength,size)
43 grid = np.array([[x,0,z] for x in pos] for z in pos])
44
45 # compute field on grid
46 B = magpy.getB(coil, grid)
47 B2 = magpy.getB(coil2, grid)
48 B_tot = B + B2
49 #conversion from mT-> G
50 B_tot *= 10
51
52 #save the data
53 np.save('B_tot.npy', B_tot)

```

Bibliography

- [And+95] M H Anderson et al. “Observation of Bose-Einstein Condensation in a Dilute Atomic Vapor”. In: *science* 269 (5221 1995), pp. 198–201. DOI: 10.1126/SCIENCE.269.5221.198. URL: https://courses.physics.illinois.edu/phys596/fa2014/StudentWork/Team3_Final.pdf.
- [And+97] M R Andrews et al. “Observation of Interference Between Two Bose Condensates”. In: *Science* 275 (5300 Jan. 1997). doi: 10.1126/science.275.5300.637, pp. 637–641. DOI: 10.1126/science.275.5300.637. URL: <https://doi.org/10.1126/science.275.5300.637>.
- [Bö+19] Fabian Böttcher et al. “Transient Supersolid Properties in an Array of Dipolar Quantum Droplets”. In: *Physical Review X* 9 (1 Mar. 2019), p. 11051. DOI: 10.1103/PhysRevX.9.011051. URL: <https://link.aps.org/doi/10.1103/PhysRevX.9.011051>.
- [Bai+16] S Baier et al. “Extended Bose-Hubbard models with ultracold magnetic atoms”. In: *Science* 352 (2016), pp. 201–205.
- [Bak+09] Waseem S Bakr et al. “A quantum gas microscope for detecting single atoms in a Hubbard-regime optical lattice”. In: *Nature* 462 (7269 2009), pp. 74–77. ISSN: 1476-4687. DOI: 10.1038/nature08482. URL: <https://doi.org/10.1038/nature08482>.
- [Chi+10] Cheng Chin et al. “Feshbach resonances in ultracold gases”. In: *Reviews of Modern Physics* 82 (2 Apr. 2010), pp. 1225–1286. DOI: 10.1103/RevModPhys.82.1225. URL: <https://link.aps.org/doi/10.1103/RevModPhys.82.1225>.
- [CI17] Gross Christian and Bloch Immanuel. “Quantum simulations with ultracold atoms in optical lattices”. In: *Science* 357 (6355 Sept. 2017). doi: 10.1126/science.aal3837, pp. 995–1001. DOI: 10.1126/science.aal3837. URL: <https://doi.org/10.1126/science.aal3837>.
- [Dav+95] K B Davis et al. “Bose-Einstein Condensation in a Gas of Sodium Atoms”. In: *Physical Review Letters* 75 (22 Nov. 1995), pp. 3969–3973. DOI: 10.1103/PhysRevLett.75.3969. URL: <https://link.aps.org/doi/10.1103/PhysRevLett.75.3969>.
- [Dem07] Wolfgang Demtröder. *Laserspektroskopie, Grundlagen und Techniken*. 5th ed. Vol. 1. 2007.

- [Dem13] Wolfgang Demtröder. *Experimentalphysik 2, Elektrizität und Optik*. 6th ed. 2013.
- [Dem18] Wolfgang Demtröder. *Experimentalphysik 1, Mechanik und Wärme*. 6th ed. 2018.
- [DJ99] B Demarco and D. S. Jin. “Onset of Fermi degeneracy in a trapped atomic gas”. In: *Science* 285 (5434 1999).
- [Foo05] Christopher J. Foot. *Atomic Physics*. 2005.
- [Guo+19] Mingyang Guo et al. “The low-energy Goldstone mode in a trapped dipolar supersolid”. In: *Nature* 574 (7778 2019), pp. 386–389. ISSN: 1476-4687. DOI: 10.1038/s41586-019-1569-5. URL: <https://doi.org/10.1038/s41586-019-1569-5>.
- [Hel55] Carl Heller. “Über die Erzeugung großräumiger homogener Magnetfelder zum Studium des Verhaltens von Magnetkompassen und Kompensiermitteln auf verschiedenen magnetischen Breiten”. In: *Deutsche Hydrografische Zeitschrift* 8 (4 1955), pp. 157–164. ISSN: 1616-7228. DOI: 10.1007/BF02019812. URL: <https://doi.org/10.1007/BF02019812>.
- [Her+21] J Hertkorn et al. “Pattern formation in quantum ferrofluids: From supersolids to superglasses”. In: *Physical Review Research* 3 (3 Aug. 2021), p. 33125. DOI: 10.1103/PhysRevResearch.3.033125. URL: <https://link.aps.org/doi/10.1103/PhysRevResearch.3.033125>.
- [Kad+16] Holger Kadau et al. “Observing the Rosensweig instability of a quantum ferrofluid”. In: *Nature* 530 (7589 2016), pp. 194–197. ISSN: 1476-4687. DOI: 10.1038/nature16485. URL: <https://doi.org/10.1038/nature16485>.
- [Klu19] Julian Kluge. “Design of a Zeeman slower for a second generation experimental setup on quantum degenerate Dysprosium gases”. University of Stuttgart, 2019.
- [LCB09] Nathan Leefer, Arman Cingöz, and Dmitry Budker. “Measurement of hyperfine structure and isotope shifts in the Dy 421 nm transition”. In: *Optics Letters* 34 (17 2009), pp. 2548–2550. DOI: 10.1364/OL.34.002548. URL: <http://www.osapublishing.org/ol/abstract.cfm?URI=ol-34-17-2548>.
- [Lid04] David R. Lide. *CRC Handbook of Chemistry and Physics*. Vol. 84. 2004.

-
- [LKL15] Erik G C P van Loon, Mikhail I Katsnelson, and Mikhail Lemeshko. “Ultralong-range order in the Fermi-Hubbard model with long-range interactions”. In: *Physical Review B* 92 (8 Aug. 2015), p. 81106. DOI: 10.1103/PhysRevB.92.081106. URL: <https://link.aps.org/doi/10.1103/PhysRevB.92.081106>.
- [Mad+00] K W Madison et al. “Vortex Formation in a Stirred Bose-Einstein Condensate”. In: *Physical Review Letters* 84 (5 Jan. 2000), pp. 806–809. DOI: 10.1103/PhysRevLett.84.806. URL: <https://link.aps.org/doi/10.1103/PhysRevLett.84.806>.
- [Mai15] Thomas Maier. “Interactions in a Quantum Gas of Dysprosium Atoms”. University of Stuttgart, 2015.
- [Maz+17] Anton Mazurenko et al. “A cold-atom Fermi–Hubbard antiferromagnet”. In: *Nature* 545 (7655 2017), pp. 462–466. ISSN: 1476-4687. DOI: 10.1038/nature22362. URL: <https://doi.org/10.1038/nature22362>.
- [Mif+06] A Miffre et al. “Atom interferometry”. In: *Physica Scripta* 74 (2 2006), pp. C15–C23. ISSN: 0031-8949. DOI: 10.1088/0031-8949/74/2/n01. URL: <http://dx.doi.org/10.1088/0031-8949/74/2/N01>.
- [Mis00] Martin Misakian. “Equations for the Magnetic Field Produced by One or More Rectangular Loops of Wire in the Same Plane”. In: *Journal of Research of the National Institute of Standards and Technology* 105 (July 2000). DOI: 10.6028/jres.105.045.
- [MS99] Harold J. Metcalf and Peter van der Straten. *Laser Cooling and Trapping*. 1999.
- [MSS54] L Marton, J Arol Simpson, and J A Suddeth. “An Electron Interferometer”. In: *Review of Scientific Instruments* 25 (11 Nov. 1954). doi: 10.1063/1.1770945, pp. 1099–1104. ISSN: 0034-6748. DOI: 10.1063/1.1770945. URL: <https://doi.org/10.1063/1.1770945>.
- [Pik+10] A Pikovski et al. “Interlayer Superfluidity in Bilayer Systems of Fermionic Polar Molecules”. In: *Physical Review Letters* 105 (21 Nov. 2010), p. 215302. DOI: 10.1103/PhysRevLett.105.215302. URL: <https://link.aps.org/doi/10.1103/PhysRevLett.105.215302>.
- [Sch+16] Matthias Schmitt et al. “Self-bound droplets of a dilute magnetic quantum liquid”. In: *Nature* 539 (7628 2016), pp. 259–262. ISSN: 1476-4687. DOI: 10.1038/nature20126. URL: <https://doi.org/10.1038/nature20126>.

- [Sch17] Matthias Schmitt. “A Self-bound Dilute Quantum Liquid of Dysprosium Atoms”. University of Stuttgart, 2017.
- [Sim+01] James C Simpson et al. “Simple Analytic Expressions for the Magnetic Field of a Circular Current Loop”. In: 2001.
- [Zuc07] Michael Zucker. “LIGO precision understated”. In: *Physics Today* 60 (5 2007).
- [Zwi+05] M W Zwierlein et al. “Vortices and superfluidity in a strongly interacting Fermi gas”. In: *Nature* 435 (7045 2005), pp. 1047–1051. ISSN: 1476-4687. DOI: 10.1038/nature03858. URL: <https://doi.org/10.1038/nature03858>.

Acknowledgments

Here I would like to acknowledge all those who made this work possible:

Zunächst möchte ich mich bei Prof. Dr. Tilman Pfau dafür bedanken, dass ich im Rahmen dieser Masterarbeit an der aktiven Forschung des 5. Physikalischen Instituts teilhaben durfte. Außerdem möchte ich mich für durchweg positive Atmosphäre und die vielen Aktivitäten des Instituts bedanken.

Mein Dank gilt außerdem Dr. Eberhard Goering für die Übernahme des Mitberichts.

I would also like to thank the entire *Dysi*-group for the great working atmosphere and a lot of great discussion whether in the lab or during lunch. Above all, I would like to thank Sean Graham, Jan-Niklas Schmidt, Jens Hertkorn and Kevin Ng for your active support during the planning and construction phase of the experimental apparatus. This was a huge team effort and soon we can all celebrate the creation of the biggest MOT the *Dysi*-group has ever seen! I would also like to thank Mingyang Guo for explaining all the intricate details of operating and locking our laser-systems.

Außerdem möchte ich mich bei Felix Kogel und Matthias Schmidt für die gemeinsame Zeit die wir seit Beginn des Studiums miteinander verbracht haben bedanken. Ob Übungsblätter lösen im dunklen Eck oder eine Limo auf den Stoinern trinken, ohne euch hätte ich dieses Studium nicht bewältigen können.

Ein besonderer Dank gilt auch Anne-Katrin Kriesch, ohne deine Hilfe bei allen Verwaltungs- und Organisationsaufgaben wäre diese Arbeit nicht möglich gewesen.

Zuletzt möchte ich mich bei meiner Familie bedanken. Ihr habt mein Studium von Beginn an unterstützt und überhaupt erst ermöglicht.

